The Astrophysical Journal, 667:97–116, 2007 September 20

BLACK HOLE MASSES AND EDDINGTON RATIOS OF AGNs AT $z < 1$: EVIDENCE OF RETRIGGERING FOR A REPRESENTATIVE SAMPLE OF X-RAY-SELECTED AGNs

L. Ballo,[1,2] S. Cristiani,[3] G. Fasano,[4] F. Fontanot,[5] P. Monaco,[5,3] M. Nonino,[3] E. Pignatelli,[4] P. Tozzi,[3] E. Vanzella,[3] A. Fontana,[6] E. Giallongo,[6] A. Grazian,[6] and L. Danese[1]

Received 2005 December 29; accepted 2007 May 1

ABSTRACT

We estimated black hole masses and Eddington ratios for a sample of X-ray-selected active galactic nuclei (AGNs) in the fields covered by the Great Observatory Origins Deep Survey (GOODS). The spanned ranges in redshift ($0.4 < z < 1$) and hard X-ray luminosity ($10^{42} \lesssim L_X \lesssim 4 \times 10^{43}$ ergs s^{-1}) allow us to study a representative subsample of the main contributors to the 2–10 keV X-ray background. Nuclear and bulge magnitudes in four bands have been measured via a two-dimensional decomposition applied to *HST* ACS images. Using the black hole versus bulge luminosity relation and the intrinsic nuclear emission, we derived the black hole mass and the AGN bolometric luminosity. We find in our sample that (1) the X-ray–to–optical indices are larger than in optically selected QSOs, as expected due to the X-ray selection); (2) the X-ray bolometric corrections are generally small, suggesting a decrease with the nuclear luminosity; (3) the Eddington ratios are about a factor 10 below the values found at higher redshift and luminosity; (4) the central black holes have rather large masses; and (5) at least for $z \lesssim 0.8$, a scarceness of black holes with mass $M_{BH} \leq 10^6\ M_\odot$ and accretion rate near the Eddington limit: this result could be ascribed to a decline in their number density, or it could suggest a substantial accretion at higher redshift ($z \gtrsim 1$) also for these smaller black holes.

Subject headings: black hole physics — galaxies: active — galaxies: nuclei — galaxies: photometry — X-rays: diffuse background — X-rays: galaxies

Online material: color figures

1. INTRODUCTION

Recent *Chandra* and *XMM-Newton* deep surveys (Brandt et al. 2001; Rosati et al. 2002; Hasinger et al. 2001) have resolved ~90% of the 2–10 keV X-ray background (hereafter XRB; see Bauer et al. 2004). The main contribution to the XRB in this energy range is due to a mixture of obscured and unobscured active galactic nuclei (AGNs), with a redshift distribution peaking at ~0.7 (Szokoly et al. 2004), and a major contribution in the interval $0.4 < z < 1$ from objects with X-ray luminosities between 3×10^{41} and 10^{43} ergs s^{-1} (Ueda et al. 2003).

The mass accreted onto the central supermassive black holes (SMBHs) of these $z < 1$ AGNs is estimated to be ~30% of the total mass density accreted at any redshift (Marconi et al. 2004; Shankar et al. 2004). An important question is whether this accreted mass is on average falling onto SMBHs already having very large mass ($\Delta M_{acc}/M_{BH} \ll 1$), or if the accretion is occurring on smaller SMBHs. The first regime corresponds to Eddington ratios $\lambda = L_{bol}/L_{Edd} \ll 1$ and can be associated with reactivation of preexisting black holes (BHs), while the latter corresponds to $\lambda \lesssim 1$ and is associated with the main episode of growth of lower mass BHs. This issue is relevant in order to reconstruct the detailed cosmic history of SMBH accretion. As an ultimate goal, one should match the mass function of the BH accreted mass with the local mass function of the quiescent BHs (see, e.g., Salucci et al. 1999; Yu & Tremaine 2002; Marconi et al. 2004; Shankar et al. 2004).

The detailed history of SMBH accretion is also a relevant clue to understand the observed relationships between the mass of local SMBHs and the mass and luminosity (Kormendy & Richstone 1995; Magorrian et al. 1998; McLure & Dunlop 2002; Marconi & Hunt 2003) or the velocity dispersion (Ferrarese & Merritt 2000; Gebhardt et al. 2000; Merritt & Ferrarese 2001; Tremaine et al. 2002) of the spheroidal component of their host galaxies. Eventually, this will cast light on physical processes involving both the SMBH and the host galaxy (Silk & Rees 1998; Granato et al. 2001, 2004; Hopkins et al. 2005).

In this paper we estimate the BH mass, the bolometric luminosity and the Eddington ratio for a representative sample of low-luminosity X-ray-selected AGNs in the redshift interval $0.4 \leq z \leq 1$.

The data demands are substantial for a study such as ours. High spatial resolution and high signal-to-noise ratio data in the X-ray produced by the *Chandra* observations in the *Chandra* Deep Fields South and North (Giacconi et al. 2002; Rosati et al. 2002; Alexander et al. 2003) are of fundamental importance to select low-luminosity AGNs. We also need optical images with excellent spatial resolution and very high quality photometry, in order to disentangle the galactic and nuclear components, and to estimate the AGN bolometric luminosity and the BH mass. In this respect the Great Observatories Origins Deep Survey (GOODS; see Giavalisco et al. 2004) is really unique; in fact, in addition to deep X-ray and optical images from the *Chandra X-Ray Observatory* and the *Hubble Space Telescope* (*HST*), it also exploits extensive follow-up work with ground-based telescopes, extending the sampling of the electromagnetic spectrum of the sources up to the radio wavelength.

[1] SISSA/ISAS, International School for Advanced Studies, 34014 Trieste, Italy; ballo@sissa.it, danese@sissa.it.

[2] European Space Astronomy Center of ESA, E-28080 Madrid, Spain; lballo@sciops.esa.int.

[3] INAF–Osservatorio Astronomico di Trieste, 34131 Trieste, Italy; cristiani@oats.inaf.it, monaco@oats.inaf.it, nonino@oats.inaf.it, tozzi@oats.inaf.it, vanzella@oats.inaf.it.

[4] INAF–Osservatorio Astronomico di Padova, 35122 Padova, Italy; fasano@pd.astro.it, pignatelli@pd.astro.it.

[5] DAUT, 34131 Trieste, Italy; fontanot@oats.inaf.it, monaco@oats.inaf.it.

[6] INAF–Osservatorio Astronomico di Roma, 00040 Monte Porzio Catone, Italy; fontana@mporzio.astro.it, giallo@mporzio.astro.it, grazian@mporzio.astro.it.

The paper is organized as follows. In § 2 (but see also Appendix A) we describe the sample selection and list the different data sets available. In § 3 we introduce the morphological analysis carried out (details are reported in Appendix B) and discuss the results of the decomposition. Section 4 is devoted to recover the nuclear properties (i.e., BH masses and nuclear bolometric luminosities). In § 5 our findings are discussed and compared with results from the literature. Finally, in § 6 we summarize our work. If not otherwise stated, throughout this paper magnitudes are given in the AB system, and hard X-ray luminosities are in the 2–8 keV energy range (when necessary, converted from $L_{2-10\,\mathrm{keV}}$ assuming a power-law X-ray spectrum with photon index $\Gamma = 1.8$: $L_{2-8\,\mathrm{keV}}/L_{2-10\,\mathrm{keV}} \simeq 0.84$). We assume a cosmology with $\Omega_M = 0.3$, $\Omega_\Lambda = 0.7$, and $H_0 = 70\,\mathrm{km\,s^{-1}\,Mpc^{-1}}$ (Spergel et al. 2003, 2007).

2. SAMPLE SELECTION

The starting point for the present work is the deep, high-resolution optical imaging performed in the F435W, F606W, F775W, and F850LP filters with the Advanced Camera for Surveys (ACS) onboard *HST* in the framework of the GOODS program. In the following, we refer to these four passbands as *B*, *V*, *i*, and *z*, respectively. GOODS covers a total area of 320 arcmin^2 in two fields centered on the *Chandra* Deep Field–South (CDF-S) and the *Chandra* Deep Field–North (CDF-N). These two regions have been targets of deep X-ray pointings (1 Ms [see Giacconi et al. 2002; Rosati et al. 2002; Alexander et al. 2003] and 2 Ms [see Alexander et al. 2003], respectively) carried out by *Chandra*. Overall, 80% of objects have redshift information. If we restrict ourselves to the CDF areas covered by GOODS, ∼98% of the X-ray objects have optical counterparts. In the GOODS north field, 63% and 17% of the X-ray sources have spectroscopic and photometric redshift, respectively; in the south area these percentages increase to 68% and 32%, respectively.

We collect all the sources in the *Chandra* X-ray catalogs lying in the GOODS fields with redshift (spectroscopic or photometric) between 0.4 and 1, and with X-ray luminosity $L_{2-8\,\mathrm{keV}} > 10^{42}$ ergs s^{-1} in order to select bona fide AGNs (Zezas et al. 1998; Moran et al. 1999). They amount to 66 sources, 88% of them having spectroscopic redshifts. The redshift interval is chosen to bracket a significant fraction of the low-luminosity sources contributing to the XRB. The upper bound $z = 1$ is imposed by the need of a sufficient signal-to-noise ratio to make a morphological analysis for most of the sources. This upper limit on the redshift also ensures that the observed *z*-band is always sampling the optical rest frame. In order to carry out the morphological analysis described in the next section, the simultaneous availability of high-quality, noncrowded *B*, *V*, *i*, and *z* ACS subimages (cutouts) is essential. This selection reduces the sample to 25 sources in the CDF-S and 28 in the CDF-N (sample A).

Full details of the selection process are given in Appendix A. Here let us note that the X-ray sources in the GOODS fields with a redshift determination cover the same region in the F_X-F_{opt} plane as the whole database of the "GOODS X-ray sources" (see Fig. 1, *top panel*), although most of the objects without redshift determination have faint optical counterpart. According to a bi-dimensional Kolmogorov-Smirnov (K-S) test, there is no evidence that the two samples are drawn from different distributions (the K-S probability is ∼60%). This makes us confident that selecting only sources with redshift determination does not induce a bias toward optically bright objects. Moreover, assuming the black hole mass–bulge luminosity relations, we can estimate how bright a bulge with a given black hole mass would be at a given redshift: in the bottom panel of Figure 1, we compare the tracks

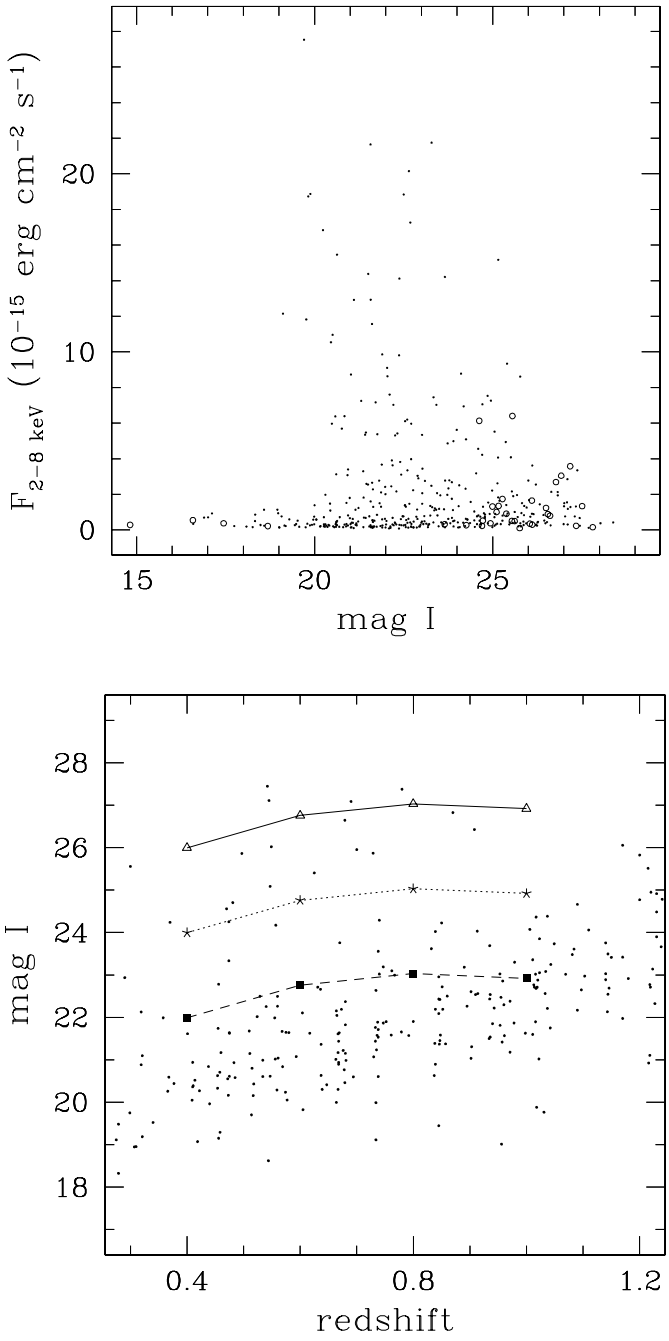

FIG. 1.—*Top:* Hard X-ray fluxes vs. *i*-band magnitudes for the X-ray sources in the GOODS fields with (*dots*) and without (*open circles*) redshift information. *Bottom: i*-band magnitudes vs. redshift for X-ray sources in the GOODS fields with redshift information, with superimposed the *i*-band magnitudes expected for bulges with black hole masses of $M_{\mathrm{BH}} = 10^5$, 10^6 and $10^7\,M_\odot$ (*from top to bottom: solid line and open triangles, dotted line and stars, and dashed line and filled squares, respectively*).

for three black hole masses (*from top to bottom,* $M_{\mathrm{BH}} = 10^5$, 10^6, $10^7\,M_\odot$) with the distribution of the optical magnitude of X-ray sources in the GOODS fields with a redshift determination. The selected range in redshift and the available magnitudes do not imply that we are forced to study only black hole with large masses.

Figure 2 shows how the sample A is distributed in redshift (*top left panel*), hard X-ray luminosity (*top right panel*), and optical magnitude (*bottom panel*). The spikes visible in the redshift distribution trace the large-scale structure identified in the whole CDF-S at $z = 0.67$ and $z = 0.73$, both in the optical (Vanzella

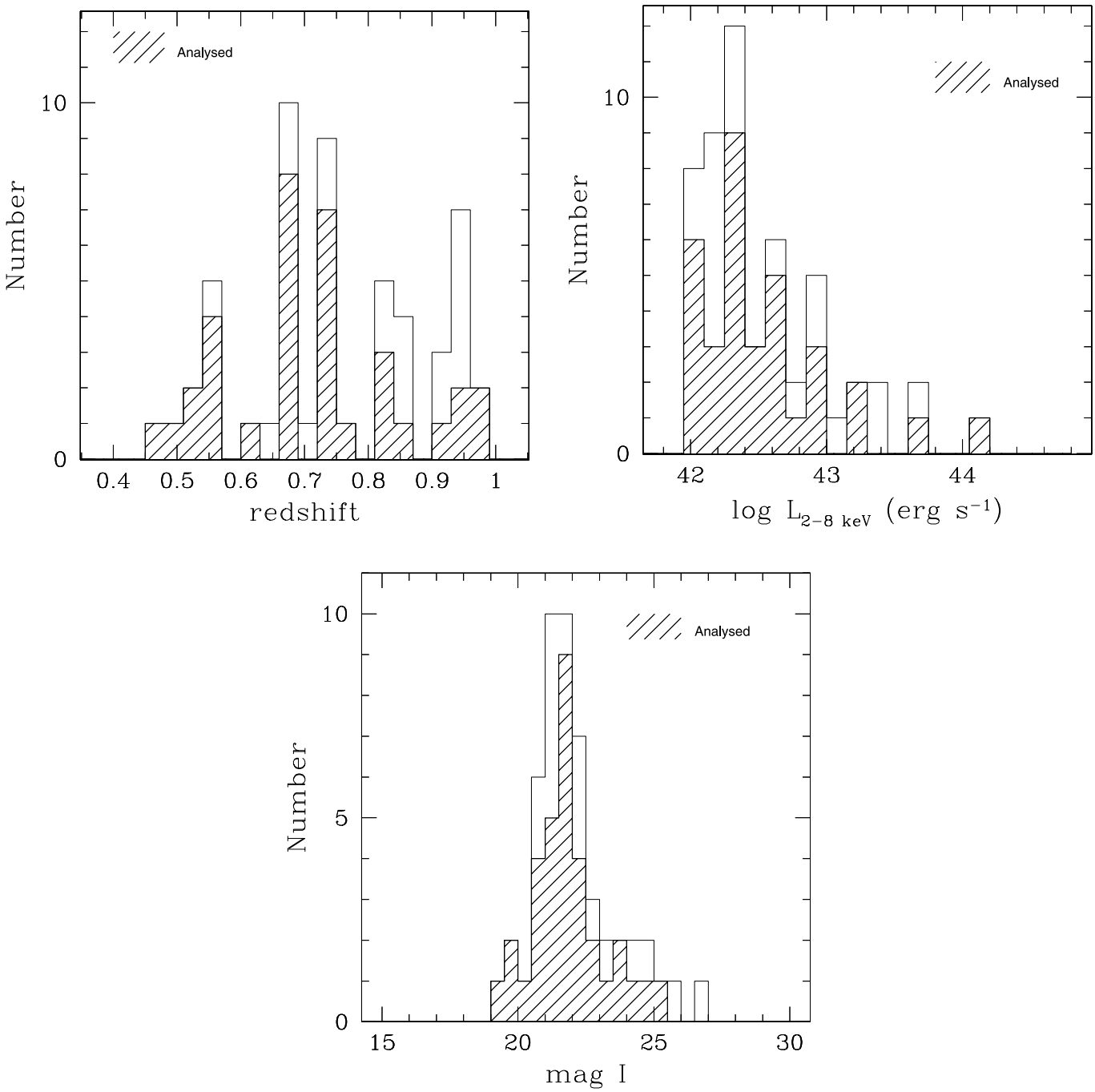

FIG. 2.—Distributions in redshift (*top left panel*), hard X-ray luminosity (*top right panel*), and *i*-band magnitude (*bottom panel*) for the sample A (GOODS X-ray sources with spectroscopic or photometric redshifts between 0.4 and 1, observed hard X-ray luminosity $L_{2-8\ keV} > 10^{42}$ ergs s^{-1}, and good cutouts in all bands; see § 2); hatched areas show the same distributions for the analyzed sources (sample B). Redshifts are from Szokoly et al. (2004), Grazian et al. (2006), and Zheng et al. (2004) for the CDF-S, and from Barger et al. (2003) for the CDF-N; luminosities are from Alexander et al. (2003); *i*-band magnitudes are from the GOODS ACS catalog (see footnote 12).

et al. 2005) and in the X-ray ranges (Gilli et al. 2003), and at $z \sim 0.85$ in the CDF-N (see Barger et al. 2003; Gilli et al. 2005).

We have removed from the sample A objects with a close companion (within a projected radius of 2″, without distinction between physical interaction or projection effect; see also Appendix B); in this way the analyzed sample (sample B) reduces to 34 objects (19 in the CDF-S and 15 in the CDF-N), listed in Table 1. As is apparent in Figure 2, the redshift and luminosity distributions of the sample B (*hatched areas*) match the distributions of the sample A, apart from a slight dearth of objects with $z \gtrsim 0.8$. According to a K-S test, we cannot prove that the two samples are drawn from different hard X-ray luminosity or redshift distributions (the K-S probabilities are 99% and 75%, respectively).

The contributions to the hard XRB[7] of the sample A is 16%.

In Figure 3 we compare the total contribution to the hard XRB computed from the CDF-S plus *ASCA* sample (Della Ceca et al. 2001; long-dashed line, with the the gray area representing the estimated uncertainties; see Tozzi 2001) with the integrated contribution of the sample A (*solid line*) and of the selected 34 sources

[7] Average total flux density in the 2-8 keV band: $(1.79 \pm 0.11) \times 10^{-11}$ ergs cm^{-2} s^{-1} deg^{-2}, from De Luca & Molendi (2004) converted from the 2–10 keV band assuming $\Gamma = 1.4$.

TABLE 1

Basic Information for X-Ray-selected AGNs (Observed $L_{2-8\,\mathrm{keV}} > 10^{42}$ ergs s^{-1}) in the GOODS Fields with $0.4 < z < 1$ Analyzed in This Work (Sample B)

R.A. (J2000.0) (1)	Decl. (J2000.0) (2)	ID (3)	Redshift (4)	$\log L_{2-8\,\mathrm{keV}}$ (ergs s^{-1}) (5)	i_{AB} (mag) (6)
		CDF-N			
12 36 18.58.....	+62 11 15.0	114	0.679	43.20	20.46
12 36 25.01.....	+62 21 15.7	141	0.747	42.29	21.87
12 36 27.75.....	+62 11 58.4	150	0.762	42.34	23.10
12 36 32.59.....	+62 07 59.8	170	0.680	42.16	21.83
12 36 35.86.....	+62 07 07.7	194	0.555	42.37	21.99
12 36 42.24.....	+62 06 12.8	222	0.857	42.60	21.38
12 36 46.33.....	+62 14 04.7	243	0.961	43.62	21.57
12 36 54.58.....	+62 11 10.6	285	0.955	42.43	22.47
12 36 59.09.....	+62 25 23.7	303	0.678	42.97	20.76
12 37 02.43.....	+62 19 26.1	323	0.514	43.27	19.70
12 37 10.07.....	+62 05 47.9	368	0.935	42.09	23.69
12 37 22.44.....	+62 05 36.1	404	0.978	42.61	21.87
12 37 24.00.....	+62 13 04.3	412	0.474	42.33	24.25
12 37 31.73.....	+62 17 03.7	439	0.839	42.61	20.89
12 37 39.46.....	+62 22 39.2	451	0.838	42.27	21.39
		CDF-S			
03 32 33.02.....	−27 45 47.4	34	0.839	42.93	22.19
03 32 26.76.....	−27 41 45.6	40	0.667	42.85	21.61
03 32 27.00.....	−27 41 05.1	42	0.734	44.17	19.12
03 32 27.61.....	−27 41 45.0	44	0.737	42.65	21.89
03 32 24.84.....	−27 56 00.0	47	0.733	42.64	21.44
03 32 24.84.....	−27 56 00.0	48	0.534	42.48	20.61
03 32 20.07.....	−27 44 47.0	51	0.670	42.35	23.76
03 32 17.18.....	−27 52 20.9	52	0.569	42.88	20.84
03 32 20.07.....	−27 44 47.0	151	0.604	42.36	22.11
03 32 08.24.....	−27 41 53.6	156	0.545	42.07	21.80
03 32 46.98.....	−27 43 46.2	170	0.664	42.14	20.00
03 32 22.51.....	−27 48 04.8	189	0.734	42.04	22.64
03 32 35.23.....	−27 53 17.8	192	0.733	42.48	21.76
03 32 39.73.....	−27 46 11.2	201	0.679	42.39	25.38
03 32 18.99.....	−27 47 55.4	252	0.481	42.13	24.71
03 32 13.92.....	−27 50 00.7	257	0.549	42.08	22.44
03 32 13.83.....	−27 45 25.6	266	0.735	42.01	21.23
03 32 34.73.....	−27 55 33.8	511	0.668	42.08	21.44
03 32 23.88.....	−27 58 42.4	613	0.910	42.29	22.54

Notes.—Cols. (1) and (2): units of right ascension are hours, minutes, and seconds, and units of declination are degrees, arcminutes, and arcseconds; col. (3): source number; col. (4): redshift for the optical counterpart, from Barger et al. (2003), Szokoly et al. (2004), Grazian et al. (2006), and Zheng et al. (2004); col. (5): *observed* X-ray luminosity in the 2−8 keV band; col. (6): AB magnitude in the *i* band from the GOODS ACS catalog (see footnote 12).

(*dashed line*): this comparison shows that with the analyzed sources we are sampling in an uniform way the same range of flux of the sample A. In summary, sample B is considered representative of the whole population of X-ray sources with spectroscopic or photometric redshifts between 0.4 and 1 and luminosity $L_{2-8\,\mathrm{keV}} > 10^{42}$ ergs s^{-1}, and only scaled (i.e., sparsely sampled) by a factor 7. Both the sample A and the analyzed objects cover the luminosity range $10^{42} \leq L_{2-8\,\mathrm{keV}} \leq 3 \times 10^{43}$ ergs s^{-1}, while only few sources exhibit larger luminosity. Taking into account the redshift and luminosity distributions, we can conclude that the sample B is representative of the AGNs contributing to the XRB at $z \leq 1$ (see, e.g., Fig. 16 in Ueda et al. 2003).

Data from *U*-band to IR, available thanks to the remarkable multiwavelength coverage of the two GOODS fields, are used to construct multiwavelength spectral energy distributions (SEDs) for the analyzed objects, see § 3:

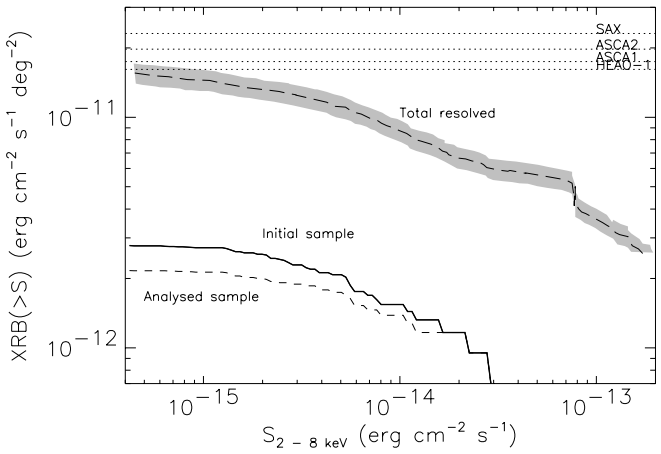

Fig. 3.—Contribution to the 2–8 keV X-ray flux density as a function of the resolved sources: comparison between (1) the total resolved contribution (*long-dashed line, with gray area representing the estimated uncertainties*) computed from the 1 Ms CDF-S sample plus the bright sample from *ASCA* (Della Ceca et al. 2001) at fluxes larger than 10^{-13} ergs cm^{-2} s^{-1}; see Tozzi (2001); (2) the contribution of our initial selection (sample A: GOODS X-ray sources with spectroscopic or photometric redshifts between 0.4 and 1, observed hard X-ray luminosity $L_{2-8\,\mathrm{keV}} > 10^{42}$ ergs s^{-1} and with good cutouts in all bands; continuous line); (3) the contribution of the analyzed sources, as in Table 1 (sample B; *dashed line*). The top dotted lines refer to previous measures of the unresolved hard X-ray background; *from bottom to top:* Marshall et al. (1980), Ueda et al. (1999), Ishisaki et al. (2001), and Vecchi et al. (1999).

CDF-S.—GOODS has imaged these fields at 3.6, 4.5, 5.8, and 8.0 μm with the Infrared Array Camera (IRAC) onboard *Spitzer*. For each field, observations have been divided into two epochs, with a mean exposure time per channel per sky pointing of approximately 23 hr per epoch (M. Dickinson et al. 2007 in preparation). In this work we will make use of the *Spitzer* data for the CDF-S as analyzed by Grazian et al. (2006). The GOODS field of the CDF-S has also been the target of a deep imaging campaign in the near-infrared with the ESO telescopes. A large field ($20' \times 20'$) has been covered with the SOFI instrument at the New Technology Telescope (NTT) in the *J* and K_s bands as part of the Deep Public Survey carried out by the ESO Imaging Survey (EIS) program; the data are described in Vandame et al. (2001). An *H*-band survey of the CDF-S, encompassing the spatial coverage of the EIS observations, has been carried out with the same instrument; the results are presented in Moy et al. (2003). The GOODS field is being covered by deeper observations in the same near-IR bands with the ISAAC instrument at the VLT. These data have been partially released by ESO and will be used in this work.[8] We also make use of *U*-band data taken with the ESO Wide Field Imager (WFI) at La Silla (Chile), which are part of the EIS public survey (Arnouts et al. 2001), as well as recent *U* images with VLT-VIMOS imager. The WFI images have been obtained in two filters, the so-called U_{35} and U_{38} filters, with an exposure time of ∼54 and ∼75 ks, respectively. The *U*-band image of VIMOS is based on a redder filter and has an exposure time of ∼10 ks. The coverage with VIMOS of the GOODS field centered on the CDF-S is partial, since the observing program has not been completed yet.

CDF-N.—In the CDF-N IR information has been collected matching our sources with the *HK′* catalog of Capak et al. (2004),

[8] The details of the ongoing GOODS program at ESO are given at http://www.eso.org/science/goods/products.html.

TABLE 2

TWO-DIMENSIONAL IMAGE FITTING MAGNITUDES

	NUCLEUS				DISK				BULGE			
ID	z	i	V	B	z	i	V	B	z	i	V	B
(1)	(2)	(3)	(4)	(5)	(6)	(7)	(8)	(9)	(10)	(11)	(12)	(13)
CDF-N												
114.....	21.66 ± 0.20	21.81 ± 0.22	21.72 ± 0.21	22.02 ± 0.28	...	...	...	...	20.52 ± 0.21	20.81 ± 0.22	22.32 ± 0.24	25.52 ± 0.25
141.....	25.57 ± 0.38	25.81 ± 0.41	26.00 ± 0.41	26.16 ± 0.43	22.84 ± 0.30	23.22 ± 0.31	24.42 ± 0.33	25.62 ± 0.34	21.71 ± 0.26	22.43 ± 0.27	23.81 ± 0.28	26.91 ± 0.36
150.....	26.66 ± 0.40	27.07 ± 0.42	27.83 ± 0.41	28.85 ± 0.50	23.90 ± 0.30	24.25 ± 0.31	25.32 ± 0.34	26.19 ± 0.36	23.15 ± 0.27	23.61 ± 0.28	25.63 ± 0.30	30.25 ± 0.35
170.....	25.82 ± 0.40	26.12 ± 0.41	26.87 ± 0.41	27.56 ± 0.43	22.90 ± 0.36	23.11 ± 0.37	23.93 ± 0.38	24.70 ± 0.41	21.72 ± 0.20	22.13 ± 0.22	23.67 ± 0.24	27.08 ± 0.24
194.....	27.67 ± 0.42	27.86 ± 0.45	28.31 ± 0.44	28.10 ± 0.48	22.25 ± 0.26	22.26 ± 0.26	23.25 ± 0.27	24.26 ± 0.28	22.63 ± 0.22	23.49 ± 0.23	24.76 ± 0.25	27.35 ± 0.29
222.....	24.59 ± 0.36	24.85 ± 0.36	25.56 ± 0.38	26.10 ± 0.41	21.78 ± 0.22	22.01 ± 0.23	23.03 ± 0.26	23.96 ± 0.26	21.58 ± 0.28	22.24 ± 0.29	24.27 ± 0.28	26.74 ± 0.31
243.....	24.43 ± 0.35	24.21 ± 0.37	24.53 ± 0.37	25.93 ± 0.39	21.55 ± 0.21	22.18 ± 0.24	23.17 ± 0.23	24.15 ± 0.25	21.66 ± 0.32	22.68 ± 0.35	24.50 ± 0.34	26.85 ± 0.37
285.....	25.83 ± 0.36	26.01 ± 0.35	26.54 ± 0.37	26.94 ± 0.38	23.00 ± 0.33	23.82 ± 0.34	25.41 ± 0.34	26.58 ± 0.35	22.01 ± 0.31	22.87 ± 0.32	24.94 ± 0.36	29.01 ± 0.37
303.....	23.93 ± 0.31	24.23 ± 0.33	23.98 ± 0.34	24.04 ± 0.36	21.47 ± 0.24	22.01 ± 0.25	22.93 ± 0.25	23.75 ± 0.26	20.98 ± 0.26	21.26 ± 0.26	22.85 ± 0.28	26.05 ± 0.30
323.....	21.58 ± 0.22	21.74 ± 0.23	21.32 ± 0.22	21.34 ± 0.25	21.86 ± 0.23	21.93 ± 0.24	22.59 ± 0.26	23.02 ± 0.28	19.80 ± 0.20	20.08 ± 0.21	21.29 ± 0.22	24.02 ± 0.24
368.....	24.61 ± 0.38	25.17 ± 0.38	26.89 ± 0.40	28.21 ± 0.43	...	...	...	...	23.25 ± 0.21	23.98 ± 0.22	25.41 ± 0.24	30.75 ± 0.28
404.....	24.52 ± 0.38	24.55 ± 0.37	25.09 ± 0.39	26.01 ± 0.40	22.11 ± 0.28	22.73 ± 0.31	23.79 ± 0.33	24.09 ± 0.34	21.83 ± 0.28	22.67 ± 0.30	24.05 ± 0.35	26.70 ± 0.38
412.....	26.52 ± 0.40	26.08 ± 0.41	26.25 ± 0.41	26.14 ± 0.43	24.33 ± 0.20	24.81 ± 0.22	25.40 ± 0.24	25.50 ± 0.24	25.21 ± 0.36	25.80 ± 0.37	26.81 ± 0.38	29.30 ± 0.41
439.....	24.27 ± 0.33	23.70 ± 0.33	23.93 ± 0.32	24.65 ± 0.35	21.46 ± 0.24	21.93 ± 0.24	22.89 ± 0.25	23.30 ± 0.27	21.01 ± 0.26	21.66 ± 0.27	23.17 ± 0.32	26.83 ± 0.33
451.....	24.57 ± 0.38	24.88 ± 0.37	25.12 ± 0.39	25.43 ± 0.40	22.73 ± 0.31	22.97 ± 0.31	24.63 ± 0.33	25.83 ± 0.36	20.87 ± 0.28	21.74 ± 0.30	23.63 ± 0.31	26.31 ± 0.35
CDF-S												
34.....	23.85 ± 0.35	24.89 ± 0.35	25.18 ± 0.36	25.20 ± 0.36	22.40 ± 0.33	22.68 ± 0.33	23.63 ± 0.34	24.17 ± 0.36	22.74 ± 0.32	23.51 ± 0.33	24.91 ± 0.36	27.87 ± 0.38
40.....	25.04 ± 0.40	25.34 ± 0.41	25.63 ± 0.43	25.84 ± 0.45	22.86 ± 0.34	23.19 ± 0.35	23.68 ± 0.35	24.58 ± 0.36	21.76 ± 0.21	21.98 ± 0.24	23.61 ± 0.28	25.90 ± 0.30
42.....	18.96 ± 0.22	19.10 ± 0.24	19.25 ± 0.26	19.36 ± 0.26	...	...	...	...	23.18 ± 0.32	24.30 ± 0.32	26.02 ± 0.35	28.68 ± 0.35
44.....	25.29 ± 0.38	25.16 ± 0.40	25.51 ± 0.43	26.04 ± 0.46	22.11 ± 0.28	22.74 ± 0.29	23.66 ± 0.31	24.78 ± 0.31	22.31 ± 0.31	22.64 ± 0.32	24.47 ± 0.33	27.59 ± 0.35
47.....	23.45 ± 0.33	23.62 ± 0.34	23.88 ± 0.36	24.57 ± 0.36	21.93 ± 0.26	22.32 ± 0.27	23.48 ± 0.27	24.04 ± 0.28	21.86 ± 0.29	22.34 ± 0.29	23.76 ± 0.30	26.52 ± 0.32
48.....	23.47 ± 0.34	23.60 ± 0.35	24.18 ± 0.35	24.36 ± 0.37	21.81 ± 0.25	22.44 ± 0.25	23.32 ± 0.27	24.69 ± 0.28	20.52 ± 0.20	20.92 ± 0.21	22.23 ± 0.21	25.10 ± 0.23
51.....	25.82 ± 0.39	25.67 ± 0.39	26.19 ± 0.41	27.42 ± 0.43	24.56 ± 0.35	24.86 ± 0.36	26.05 ± 0.37	27.67 ± 0.39	24.02 ± 0.28	24.23 ± 0.30	26.10 ± 0.32	27.91 ± 0.35
52.....	23.02 ± 0.35	22.88 ± 0.34	23.59 ± 0.35	23.57 ± 0.38	20.90 ± 0.23	21.33 ± 0.24	22.08 ± 0.26	24.38 ± 0.28	22.21 ± 0.30	23.05 ± 0.32	24.31 ± 0.33	26.56 ± 0.33
151.....	25.41 ± 0.38	25.48 ± 0.38	26.14 ± 0.39	26.67 ± 0.42	22.59 ± 0.30	23.30 ± 0.30	24.18 ± 0.32	25.35 ± 0.34	22.16 ± 0.24	22.64 ± 0.24	23.99 ± 0.26	27.04 ± 0.28
156.....	25.54 ± 0.39	25.96 ± 0.38	25.66 ± 0.40	25.83 ± 0.43	23.26 ± 0.34	23.37 ± 0.35	24.61 ± 0.37	24.57 ± 0.38	21.72 ± 0.19	21.85 ± 0.20	22.97 ± 0.20	25.39 ± 0.22
170.....	25.97 ± 0.40	25.02 ± 0.41	26.11 ± 0.41	25.92 ± 0.44	21.18 ± 0.23	21.64 ± 0.24	22.71 ± 0.26	23.84 ± 0.27	19.85 ± 0.22	20.27 ± 0.24	21.60 ± 0.25	24.05 ± 0.27
189.....	26.01 ± 0.38	26.21 ± 0.39	26.47 ± 0.39	27.20 ± 0.41	24.02 ± 0.35	24.57 ± 0.38	25.09 ± 0.38	26.60 ± 0.39	22.25 ± 0.28	22.89 ± 0.30	24.84 ± 0.30	27.46 ± 0.32
192.....	25.56 ± 0.39	25.72 ± 0.40	25.91 ± 0.42	26.60 ± 0.44	22.20 ± 0.30	22.80 ± 0.30	23.76 ± 0.31	24.67 ± 0.32	21.81 ± 0.27	22.27 ± 0.28	24.01 ± 0.31	26.65 ± 0.33
201.....	25.77 ± 0.33	25.58 ± 0.35	25.52 ± 0.37	25.62 ± 0.38	...	...	...	...	26.85 ± 0.37	27.34 ± 0.38	29.06 ± 0.38	30.58 ± 0.39
252.....	25.76 ± 0.35	26.29 ± 0.33	25.84 ± 0.34	26.12 ± 0.34	...	...	...	...	24.62 ± 0.19	25.04 ± 0.20	26.49 ± 0.23	28.01 ± 0.26
257.....	26.68 ± 0.40	26.51 ± 0.40	27.01 ± 0.41	27.57 ± 0.42	23.27 ± 0.34	23.11 ± 0.34	23.37 ± 0.36	24.16 ± 0.36	22.81 ± 0.25	23.31 ± 0.26	25.06 ± 0.28	27.04 ± 0.30
266.....	24.92 ± 0.37	25.80 ± 0.38	25.94 ± 0.37	26.54 ± 0.40	21.35 ± 0.23	21.89 ± 0.23	22.64 ± 0.25	23.40 ± 0.27	21.91 ± 0.28	22.14 ± 0.28	23.94 ± 0.29	26.80 ± 0.30
511.....	24.73 ± 0.37	24.39 ± 0.37	24.61 ± 0.39	25.24 ± 0.40	22.17 ± 0.30	22.66 ± 0.30	23.99 ± 0.33	25.05 ± 0.34	21.58 ± 0.25	21.98 ± 0.26	23.41 ± 0.26	27.10 ± 0.29
613.....	24.43 ± 0.37	25.35 ± 0.37	26.01 ± 0.39	27.83 ± 0.40	22.50 ± 0.25	23.11 ± 0.26	24.02 ± 0.26	24.75 ± 0.27	22.91 ± 0.30	23.67 ± 0.30	25.77 ± 0.33	28.09 ± 0.34

NOTES.—Col. (1): source number, as in Table 1; cols. (2)–(5): total magnitude (not corrected for Galactic extinction) of the PSF component in the *HST* filters z, i, V, and B, respectively; cols. (6)–(9): total magnitude (not corrected for Galactic extinction) of the *exponential* component in the *HST* filters z, i, V, and B, respectively; cols. (10)–(13): total magnitude (not corrected for Galactic extinction) of the de Vaucouleurs component in the *HST* filters z, i, V, and B, respectively. Errors are quoted at a 68% of declared confidence level (see Appendix B for details).

covering an area of 0.1 deg^2 centered on the CDF-N. The *HK′* filter covers both the *H* and *K′* bands in a single filter; it allows a greater depth but involves some loss of color information. *HK′* data have been collected using the *QUIRC* camera on the University of Hawaii 2.2 m telescope, with a $3.6' \times 3.6'$ field of view and with an AB magnitude limit across the field of 22.1 (in a $9' \times 9'$ field around the CDF-N the band reaches a limit of 22.8 mag).

3. DATA ANALYSIS

In order to disentangle the main galactic components (nucleus, bulge, and disk) for the AGNs in our sample, we adopt a two-dimensional fitting approach, applied to the GOODS *HST* ACS images. In particular, to separate a typically faint nucleus from the surrounding bright bulge, we need to determine accurate and quantitative morphological information. It has been shown that modeling in two dimensions allows a better estimate of the parameter values in a bulge-disk decomposition (e.g., Byun & Freeman 1995; Wadadekar et al. 1999). To perform the fit we use the two-dimensional image decomposition program GALFIT (Peng et al. 2002). A galaxy model is applied, composed by a bulge, a disk, and a nuclear source. The details of the procedure, as well as how we estimated the errors associated with the magnitudes of the different components, are presented in Appendix B. Here we want to stress that in our surface photometry decomposition we take advantage of images in four different bands, in which the components of the host galaxy have a different relative importance. Results for the 34 sources analyzed are reported in Table 2 (magnitudes of the nucleus in cols. [2]–[5]; magnitudes of the disk in cols. [6]–[9]; and magnitudes of the bulge component in cols. [10]–[13]) and Table 3 (the host galaxy morphological parameters, i.e., scale length, position angle, and ratio of the semiminor axis to the semimajor axis for the disk are given in cols. [3]–[5] and for the bulge in cols. [6]–[8]).

In Figure 4*a* we show as an example the result of the decomposition in a typical case (ID 34, CDF-S; $z = 0.839$). Similar images for all the analyzed sources are presented in the electronic edition. The residuals after subtracting the final model (*bottom panels*) from the original images (*top panels*) in the four bands show that the object is well modeled, apart from the residuals tracing the spiral arms (never accounted for in the applied galaxy model) and some particularly intense spots of emission.

Since the analysis is carried out *separately* in the four bands, no a priori constraint is imposed on the measured spectral energy distributions for the individual components: bulge, disk, and nucleus. It is worth recalling that reddening may significantly affect the observed SEDs. Intrinsic nuclear emission in the UV and optical ranges may be altered by dust absorption from circumnuclear and/or more diffuse component(s). The latter is also relevant for the galactic components, particularly for the disk, which is composed by younger and bluer stars.

Bearing this in mind, as a first test of the goodness of our analysis we compare the resulting SEDs with suitable templates. SED templates for the bulge have been derived using a set of single stellar population (SSP) SEDs.[9] From this set of SEDs we select a template representing the "typical" elliptical galaxy at $z \sim 0$, by comparison with a mean local spectrum (obtained from the observed ones of NGC 1399 and NGC 1404; A. Bressan 2005, private communication). To take into account the well-known metallicity-age degeneracy, we assume two initial chemical compositions of the evolutionary sequences: [$Z = 0.02$, $Y = 0.28$], and [$Z = 0.05$, $Y = 0.352$], where Z is the mass fraction of heavy elements in the interstellar gas and Y is the fraction by mass of helium (the solar values are $Z_\odot = 0.02$ and $Y_\odot = 0.21$). For both metal contents, integrated spectra of SSP of different ages have been compared with the mean empirical spectrum, finding the age that provides the best agreement: 10 Gyr for $Z = 0.05$, and 11 Gyr for $Z = 0.02$. For the two metallicities, having fixed the epoch of formation, we compute the integrated SSP spectrum at the redshift of each analyzed source. While for the bulge component we assumed that stars formed in a single burst, for the SEDs of the disk component we assumed a continuous star formation during its life. The SSPs used are the same as for the bulge. Finally, to check the nuclear optical SED, we adopt the QSO template spectrum of Cristiani & Vio (1990) down to 538 Å, modified as described by Cristiani et al. (2004) and Monaco & Fontanot (2005) and extrapolated to 300 Å using $f_\nu \propto \nu^{-1.75}$ (following Risaliti & Elvis 2004).

[9] Available at http://web.pd.astro.it/granato/grasil/SSP/ssp.html; see also Silva et al. (1998).

TABLE 3
TWO-DIMENSIONAL IMAGE FITTING MORPHOLOGICAL PARAMETERS

		Disk			Bulge		
ID (1)	Redshift (2)	r_d (3)	P.A. (deg) (4)	b/a (5)	r_e (6)	P.A. (deg) (7)	b/a (8)
CDF-N							
114.....	0.679	...	...	...	1.57	−6.62	0.87
141.....	0.747	6.38	−20.54	0.99	8.61	−19.36	0.95
150.....	0.762	3.59	−16.31	0.65	5.26	−21.31	0.62
170.....	0.680	2.77	−9.47	0.32	7.09	−8.47	0.91
194.....	0.555	0.39	−41.96	0.93	1	−43.96	0.99
222.....	0.857	7 0.09	49.34	0.52	11.51	48.85	0.57
243.....	0.961	1.38	58.78	0.77	4.01	60.30	0.80
285.....	0.955	1.05	42.38	0.84	6	41.38	0.86
303.....	0.678	2.08	58.11	0.43	3.46	59.00	0.53
323.....	0.514	3.19	−86.18	0.81	4.09	−88.77	0.76
368.....	0.935	...	...	...	1.86	...79.85	0.68
404.....	0.978	10.27	−0.79	0.40	10.60	−2.79	0.50
412.....	0.474	0.51	−54.11	0.35	0.81	−56.33	0.31
439.....	0.839	3.01	84.41	0.79	3.90	83.90	0.86
451.....	0.838	1.54	20.62	0.48	2.36	19	0.52
CDF-S							
34.....	0.839	1.28	−7.22	0.48	4.59	−6.22	0.46
40.....	0.668	0.24	−43.84	0.85	0.97	−56.30	0.87
42.....	0.734	...	...	...	1.40	−20.30	0.55
44.....	0.734	1.37	−2.07	0.68	1.32	−2.70	0.67
47.....	0.733	0.62	25.96	0.86	1.27	36.17	0.96
48.....	0.534	10.00	48.40	0.82	10.23	62.10	0.82
51.....	0.670	1.21	−57.39	0.80	0.64	−51.41	0.66
52.....	0.569	0.81	−55.89	0.80	2.40	−53.23	0.77
151.....	0.604	1	−69.09	0.28	2.37	−70.40	0.26
156.....	0.545	4.95	−16.24	0.79	5.41	−14.24	0.76
170.....	0.664	1.58	33.21	0.52	4.56	32.91	0.53
189.....	0.734	4.08	−56.78	0.30	3.27	−54.78	0.32
192.....	0.735	1.28	−19.12	0.50	2.50	17.88	0.52
201.....	0.679	...	...	...	1.20	21.36	0.33
252.....	0.481	...	...	...	0.45	−27.36	0.60
257.....	0.549	2.21	3.38	0.31	2.12	3.27	0.27
266.....	0.735	3.79	−21.12	0.26	2.95	−20.80	0.27
511.....	0.668	4.78	16.97	0.93	5.14	18.97	0.90
613.....	0.910	4.29	43.99	0.44	6.39	44.59	0.57

NOTES.—Col. (1): source number, as in Table 1; col. (2): redshift for the optical counterpart, as in Table 1; cols. (3)–(5): scale length, position angle, and semiminor axis to semimajor axis ratio of the exponential disk; cols. (6)–(8): scale length, position angle, and semiminor axis to semimajor axis ratio of the de Vaucouleurs law.

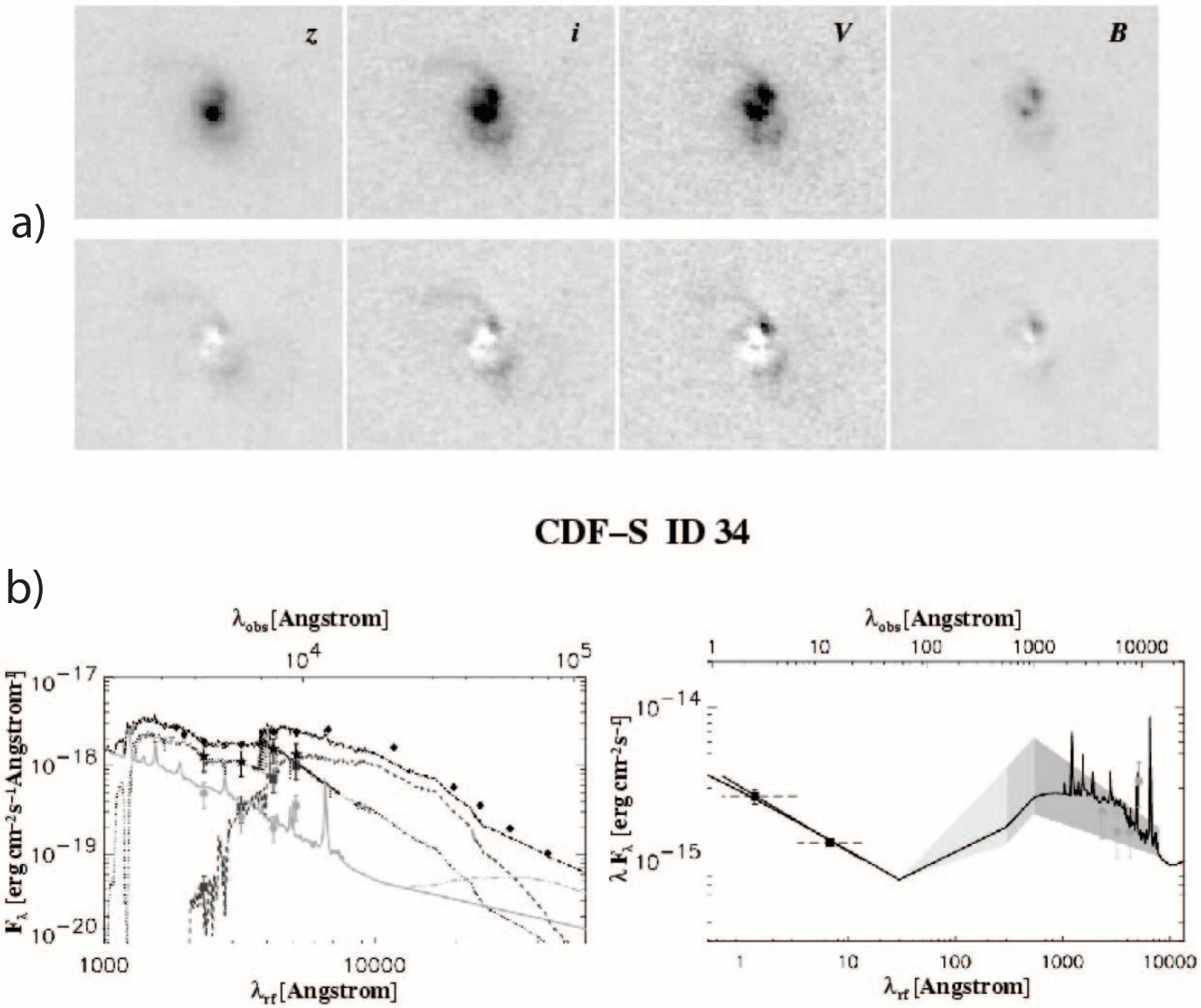

FIG. 4.—Result of the analysis for a typical case [ID 34, CDF-S; $z = 0.839$]. (*a*) Original images in the four bands (*top panels*) and residuals after subtracting the final model from the original images (*bottom panels*; see § 3 and Appendix B). (*b*) *Left panel:* Fit of the templates (bulge, *dashed line*; disk, *dotted line*; nucleus, *solid line*) to the decomposed optical magnitudes for the different components (bulge, *squares*; disk, *stars*; and nucleus, *circles*), and comparison of the sum of the templates (*dot-dashed line*) with the fluxes observed from the whole galaxy in all the available bands (*diamonds*); a contribution from a circumnuclear torus (*long-dashed line*), adapted from the mean SED of a typical Seyfert 1 galaxy reported in Granato & Danese [1994]), is assumed to account for *Spitzer* data. *Right panel:* Fit of the QSO template (*solid line*) to the nuclear SED (optical magnitudes, *circles*; and X-ray flux, *squares*; gray areas represent the uncertainty in the optical emission, estimated as described in § 4.2, and the consequent uncertainty in the UV range). [*See the electronic edition of the Journal for a color version of this figure.*]

In Figure 4*b* (*left panel)* we show the comparison of the decomposed SEDs with the three templates and the magnitudes for the whole galaxy in all the available bands for a generic case (ID 34, CDF-S; $z = 0.839$). The same comparison for the whole sample is shown in the electronic edition. For the bulge component the observed SEDs are in good agreement with the template (χ^2 per degree of freedom between 0.8–0.9 and 1.3–1.5). We stress that the bulge component is expected to be less affected by absorption. Even for the disk component very good agreement is generally found, without invoking large correction for absorption.

Concerning the nuclei, the agreement of the observed SEDs with the template is good for 70% of the analyzed objects; in the remaining 10 cases the emission in the *V* and especially *B* bands is lower than expected from the SED normalized to the *i* and *z* bands. The presence of significant obscuration around these nuclei is confirmed by their high column density, $N_H \geq 10^{22}$ cm^{-2}, inferred from their X-ray emission.

Fluxes from the decomposition and templates have also been compared with the magnitudes for the whole galaxy recovered from the GOODS catalog, as well as with the magnitudes in the IR (including data from *Spitzer*) and *U* band, when available. For the *U*-band and *Spitzer* data the angular resolution is not good enough to let us to make a morphological decomposition. Nevertheless, we can obtain important indications by comparing the observed total fluxes with the sum of the templates of bulge, disk,

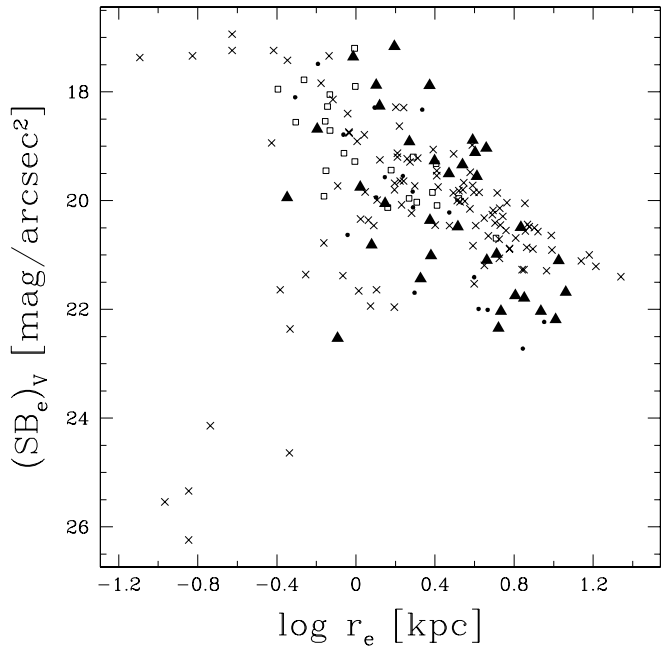

FIG. 5.—Average surface brightness within the effective radius in the *V*-band (Johnson magnitude) vs. the effective radius. The surface brightness for each bulge hosting an X-ray-selected AGNs (*triangles*) has been derived from the parameters reported in Table 2 and Table 3 (with a *K*-correction applied to convert the observed *i*-band AB magnitudes in rest-frame *V*-band Johnson magnitudes). The distribution found for the analyzed sources is in good agreement with that of local elliptical galaxies and bulges studied by Bender et al. (1992) converted in the *V* band assuming $B - V = 0.96$ and corrected for the different cosmology adopted (*crosses in the figure*). The same region in the SB_e-r_e plane is occupied by the 18 bulges of Seyfert 1 and Seyfert 1.5 galaxies observed in the *V*-band by Granato et al. (1993), corrected for the different cosmology adopted (*dots*). We also find a good agreement with the distribution reported by Fasano et al. (1998) for a sample of 23 early-type galaxies with spectroscopic redshift $z \lesssim 3.4$, with *K*- and evolutionary corrections applied (see their Fig. 6) and corrected for the different cosmology adopted (*open squares*).

and nucleus, normalized to the decomposed magnitudes. In particular, we are able to reproduce the *Spitzer* data by assuming a contribution from a circumnuclear torus, as observed in a typical Seyfert 1 galaxy (see Granato & Danese 1994).

The constraints derived from the observed IR emission for the flux expected on the basis of this reconstruction are particularly important when the nuclear component is dominant and tends to overwhelm the emission from the host galaxy: in these cases the magnitudes determined for bulge and disk are not completely reliable, and this may affect the BH mass determination (see § 4.1). As described in more detail in § 3.1, in such cases we can only provide upper limits for the bulge magnitudes; constraints imposed by the observations in the IR range prevent us from *overestimating* this fainter component.

The bulge component is relevant not only in the estimate of the nuclear contribution, but also in determining the BH masses (see § 4). Therefore, we checked that the relation between the effective radius r_e and the surface brightness within it, SB_e, is consistent with that derived for local samples. In particular, from Figure 5 it is apparent that the bulges derived through our analysis are distributed in the r_e-SB_e plane as the sample of nearby elliptical galaxies and bulges studied by Bender et al. (1992). It is interesting to note that the same region of the plane is occupied by the bulges of local Seyfert galaxies, as determined by Granato et al. (1993), as well as by a sample of early-type galaxies at higher redshift (see Fasano et al. 1998).

3.1. *Host-dominated and Nucleus-dominated Sources*

When the optical images are dominated at all wavelengths by one of the galaxy components (nucleus, bulge, or disk), the other components cannot be tightly constrained.

In sources dominated by the AGN (two objects in the present sample), we can only put upper limits to the host component by minimizing the nuclear contribution (which is well constrained). We put a threshold on the nucleus-to-total luminosity ratio N/T (reported in Table 4) in the *z* band of $N/T(z) = 0.2$ as a fiducial value to identify the galaxies affected by this problem. For the two analyzed sources satisfying this criterion (ID 42, CDF-S, $N/T(z) = 0.329$; and ID 201, CDF-S, $N/T(z) = 0.293$),we proceed as follows.

1. We assume for the QSO template a normalization 2 σ lower than the best fit (where the uncertainties are evaluated as described in Appendix B), determining a minimum value for the nuclear magnitudes in the four bands.
2. Assuming these nuclear magnitudes, we rescale the bulge component[10] until the observed value of the total fluxes is reached.
3. Finally, we compare the new galaxy reconstruction (i.e., the sum of the templates of bulge and nucleus rescaled) with the emission in the IR bands, checking that the new estimate does not overpredict (at more than 2 σ level) the emission at wavelengths greater than 1 μm.

For both sources we find that the bulge luminosity can increase up to a factor of 10 with respect to the result of the decomposition. We consider these values robust upper limits.

On the other hand, when the optical emission is dominated by the host galaxy components (bulge and/or disk, six objects), the nuclear contribution provided by GALFIT could be a lower limit to the actual one. We reanalyzed separately the six sources with nucleus-to-total luminosity ratio in the *V* band $N/T(V) < 0.05$ (see Table 4).

1. We assume for bulge and disk templates a normalization 2 σ lower than the best fit (where the uncertainties are evaluated as described in Appendix B), determining a minimum value for their magnitudes in the four bands.
2. Upper limits to the nuclear magnitudes are then calculated imposing that the total (host plus nucleus) values are equal to the observed ones.
3. We check that the new estimate of the nucleus in the *U* band is not higher (at more than 2 σ level) than the observed flux.

Again, the results of this procedure are considered robust upper limits to the nuclear luminosity.

4. RECOVERING THE NUCLEAR PROPERTIES

Disentangling the different galactic components as described in § 3 and in Appendix B provides detailed information on the bulge and nuclear luminosity. This information is relevant in order to study the nuclear activity of the galaxies in our sample. In § 4.1 we present our derivation of the BH mass, while the bolometric luminosity is evaluated from optical and X-ray nuclear luminosities as described in § 4.2.

4.1. *Black Hole Masses*

Starting from the absolute magnitudes of the bulge component, we obtain an estimate of the mass of the central compact object,

[10] We note that for both the sources reanalyzed the disk component is not requested in the fit.

TABLE 4

Ratio of the Different Components Magnitudes, as Obtained from the Two-dimensional Image Fitting

		Bulge/Galaxy				Nucleus/Bulge				Nucleus/Total			
ID	Redshift	z	i	V	B	z	i	V	B	z	i	V	B
(1)	(2)	(3)	(4)	(5)	(6)	(7)	(8)	(9)	(10)	(11)	(12)	(13)	(14)
CDF-N													
114	0.679	1.000	1.000	1.000	1.000	0.349	0.396	1.739	25.26	0.115	0.124	0.241	0.325
141	0.747	0.739	0.675	0.636	0.234	0.029	0.045	0.133	1.986	0.020	0.028	0.068	0.194
150	0.762	0.666	0.643	0.428	0.022	0.040	0.041	0.132	3.631	0.024	0.025	0.048	0.065
170	0.680	0.747	0.712	0.560	0.101	0.023	0.025	0.052	0.643	0.016	0.017	0.027	0.054
194	0.555	0.413	0.245	0.200	0.055	0.010	0.018	0.038	0.501	0.004	0.004	0.007	0.025
222	0.857	0.546	0.447	0.242	0.072	0.063	0.091	0.305	1.809	0.031	0.036	0.060	0.093
243	0.961	0.476	0.386	0.227	0.077	0.078	0.245	0.972	2.323	0.033	0.074	0.133	0.116
285	0.955	0.714	0.705	0.605	0.097	0.030	0.055	0.229	6.742	0.020	0.035	0.098	0.221
303	0.678	0.610	0.667	0.518	0.107	0.066	0.065	0.354	6.362	0.036	0.038	0.118	0.224
323	0.514	0.870	0.846	0.768	0.285	0.194	0.218	0.967	11.805	0.112	0.119	0.230	0.303
368	0.935	1.000	1.000	1.000	1.000	0.286	0.336	0.257	10.365	0.100	0.112	0.093	0.313
404	0.978	0.565	0.515	0.441	0.083	0.084	0.177	0.383	1.905	0.041	0.072	0.112	0.107
412	0.474	0.309	0.287	0.214	0.029	0.298	0.774	1.676	18.345	0.072	0.133	0.173	0.205
439	0.839	0.602	0.560	0.436	0.037	0.050	0.153	0.495	7.399	0.027	0.068	0.131	0.151
451	0.838	0.847	0.756	0.715	0.391	0.033	0.056	0.254	2.254	0.026	0.038	0.118	0.242
CDF-S													
34	0.839	0.422	0.318	0.235	0.032	0.360	0.280	0.777	11.665	0.104	0.070	0.118	0.176
40	0.668	0.734	0.753	0.516	0.229	0.049	0.045	0.156	1.057	0.032	0.031	0.065	0.140
42	0.734	1.000	1.000	1.000	1.000	48.591	119.994	511.588	5323.043	0.329	0.331	0.333	0.333
44	0.734	0.454	0.523	0.322	0.070	0.064	0.098	0.384	4.169	0.027	0.044	0.090	0.155
47	0.733	0.516	0.495	0.436	0.092	0.231	0.308	0.895	6.026	0.088	0.105	0.180	0.209
48	0.534	0.766	0.802	0.732	0.407	0.066	0.085	0.166	1.977	0.044	0.056	0.089	0.236
51	0.670	0.622	0.641	0.488	0.445	0.191	0.265	0.920	1.570	0.087	0.113	0.191	0.226
52	0.569	0.231	0.170	0.114	0.118	0.474	1.170	1.941	15.785	0.083	0.125	0.133	0.283
151	0.604	0.599	0.649	0.544	0.174	0.050	0.073	0.138	1.404	0.027	0.041	0.061	0.141
156	0.545	0.805	0.802	0.818	0.318	0.030	0.023	0.085	0.668	0.022	0.017	0.057	0.130
170	0.664	0.773	0.780	0.736	0.450	0.004	0.013	0.016	0.181	0.003	0.010	0.011	0.065
189	0.734	0.836	0.825	0.557	0.310	0.031	0.047	0.223	1.273	0.024	0.035	0.091	0.181
192	0.735	0.588	0.619	0.441	0.139	0.032	0.042	0.175	1.047	0.018	0.024	0.063	0.101
201	0.679	1.000	1.000	1.000	1.000	2.723	5.054	26.065	96.235	0.268	0.294	0.325	0.331
252	0.481	1.000	1.000	1.000	1.000	0.348	0.318	1.813	5.721	0.114	0.108	0.244	0.299
257	0.549	0.605	0.454	0.175	0.066	0.028	0.052	0.165	0.616	0.016	0.022	0.027	0.036
266	0.735	0.374	0.443	0.233	0.042	0.063	0.034	0.158	1.267	0.022	0.015	0.033	0.046
511	0.668	0.634	0.652	0.630	0.132	0.055	0.107	0.331	5.516	0.031	0.058	0.128	0.229
613	0.910	0.407	0.375	0.166	0.044	0.247	0.212	0.801	1.275	0.077	0.064	0.095	0.048

Notes.—Col. (1): source number, as in Table 1; col. (2): redshift for the optical counterpart, as in Table 1; cols. (3)–(6): bulge-to-galaxy ratio in the four bands; cols. (7)–(10): nucleus-to-bulge ratio in the four bands; cols. (11)–(14): nucleus-to-total ratio in the four bands.

exploiting the observed local relationship between BH mass and bulge component luminosity. Several versions of this relation have been proposed with the bulge luminosity evaluated at electromagnetic bands ranging from B to K (see, e.g., Kormendy & Gebhardt 2001; McLure & Dunlop 2002; Marconi & Hunt 2003).

In order to compute the BH mass, we assume that (1) in this relation the absolute magnitude of the bulge strictly mirrors the mass in old stars, $M_{\rm bulge}$, which is the quantity primarily related to the BH mass; and (2) the $M_{\rm bulge}$-$M_{\rm BH}$ relation is imprinted at high redshift, driving the main episode of accretion.

The latter hypothesis is supported by the findings of Peng et al. (2006), who show that the $M_{\rm BH}$-M_R relations for five AGNs at $z \leq 1$ are compatible with the local relation, once passive evolution of the stellar population is allowed for, and by McLure & Dunlop (2002), who, analyzing with the same technique a sample of 72 active galaxies (Seyfert galaxies and QSOs) at $z \lesssim 0.5$, demonstrate that AGN host galaxies at these redshifts follow a relation between BH mass and bulge luminosity consistent with that of local quiescent galaxies. There are claims that the correlation between BH mass and bulge velocity dispersion could be subject to a cosmic evolution (Woo et al. 2006); however, such a behavior would produce BH mass estimates slightly higher than that presented in the following. On the other hand, it is hard to imagine how a significant independent evolution can lead to a $M_{\rm bulge}$-$M_{\rm BH}$ relation with a scatter as small as that reported e.g., by Ferrarese & Ford (2005).

The relation with the total R-band magnitude of the bulge reported in McLure & Dunlop (2002) for a sample of 20 inactive E-type galaxies at $z \sim 0$ and converted to $H_0 = 70$ km s^{-1} Mpc^{-1} reads

$$\log\left(\frac{M_{\rm BH}}{M_\odot}\right) = -0.50(\pm 0.03)M_R - 2.69(\pm 0.72), \quad (1)$$

with a scatter of $\Delta \log (M_{\rm BH}) = 0.33$. The $M_{\rm bulge}$-$M_{\rm BH}$ relation reported by Bettoni et al. (2003) in their equation (1) for a sample

of nearby inactive ellipticals is in good agreement with equation (1), once the different cosmology is taken into account (even if in this second case the scatter is larger, 0.39 dex). It is worth noting that equation (1) has been derived using *B*- and *V*-band magnitudes, translated to *R* band assuming average colors $(B-R)=1.57$ and $(V-R)=0.61$. The relation reported by Marconi & Hunt (2003) exploits the *K*-band magnitudes and on average predicts BH masses higher by about 0.3 dex at fixed luminosity. The difference could be ascribed to the uncertainty in evaluating the bulge component of spiral galaxies of the observed sample (Shankar et al. 2004). The relationship estimated by Kormendy & Gebhardt (2001) using *B*-band bulge luminosities yields BH masses larger at most by about 0.2 dex than those predicted on the basis of equation (1). On the other hand, Bernardi et al. (2007) and Tundo et al. (2006) have suggested that the $M_{\rm BH}$-L relation is biased toward predicting more massive black holes for a given luminosity. The intrinsic $M_{\rm BH}$-L relation proposed by Bernardi et al. (2007) in the range of luminosities of interest for the present work yields BH masses that are very close to the corresponding ones of equation (1) ($\Delta \log M_{\rm BH} \leq 0.2$).

In the following we conservatively adopt the relation proposed by McLure & Dunlop (2002), which yields the lowest mass estimates. The BH masses quoted in the following could be a factor of 1.5–2 higher (and, correspondingly, the Eddington ratios lower by the same factor), if the relationships proposed by Kormendy & Gebhardt (2001) or by Marconi & Hunt (2003) were used.

In order to estimate the rest-frame *R*-band magnitude at $z \sim 0$ for the bulges in our sample, we started from the SSP SEDs normalized as described in § 3 (*K*-correction) and computed their passive evolution up to the present epoch.[11] The *R*-band magnitudes obtained by using the two metallicities introduced in § 3 are very similar, within 0.1 mag for all the sources. The mean of the *R*-band magnitudes, as well as the BH masses obtained from equation (1), are reported in Table 5. For sources dominated by the nuclear component or by the host galaxy, the same fit has been also carried out assuming for the bulge the magnitudes recovered as described in § 3.1. The corresponding upper or lower limit to the mass of the central BH is reported as a second line in Table 5.

Errors for the *R*-band magnitude of the bulge component are evaluated by quadratically summing two different contributions:

1. The uncertainties associated with the decomposed magnitudes propagate on to the best-fit normalization of the elliptical template adopted in computing the *R*-band magnitudes: for each source, we repeat the fit changing the normalization of the template until $\Delta\chi^2 = 1$, and we compute the *R*-band magnitudes corresponding to the minimum and maximum values of the normalization.
2. The difference between the *R*-band magnitudes found by using for the SSPs two different metallicities (see § 3) is assumed as an estimate of the error induced by selecting that particular templates to represent a local inactive galaxy (i.e., by choosing the two above-mentioned pairs age/metallicity).

When propagated to yield the uncertainties of the BH masses, the contribution due to the error in M_R is always negligible with respect to the scatter in the relation described by equation (1).

The masses are distributed over two decades, $2\times10^6 \leq M_{\rm BH} \leq 2.5\times10^8\ M_\odot$; only 3 out of 34 objects have $M_{\rm BH} \leq 10^6\ M_\odot$. AGNs at low redshift span the whole range in mass, while at the upper end of the redshift distribution only large ($M_{\rm BH} > 10^7\ M_\odot$) BH masses are found (see Fig. 6, *top panels*). No obvious selection effects, in this regard, have been identified. Such a behavior seems to be an intrinsic property of the sample. We do not see any correlation between the estimated bulge luminosity and the X-ray luminosity. As a consequence, no correlation is found also between BH mass and X-ray luminosity.

[11] As a check, we evaluated also the BH masses obtained from the relation for AGNs at higher redshift (see Table 3 in McLure & Dunlop 2002) using the rest-frame *R*-band magnitude at the redshift of each source (i.e., *without evolution*); we found a systematic shift of the order of +0.18 dex with respect to the values reported in Table 5.

4.2. *Nuclear Bolometric Luminosities*

In order to gain insight into the accretion rates powering these sources, we need to investigate their nuclear bolometric luminosity. We compare the nuclear emission (i.e., the X-ray flux, totally ascribed to the AGN, and the optical nuclear magnitudes) to SEDs of active nuclei with different X-ray–to–optical ratios. In these SEDs, the high-energy emission is described as a power law with photon index Γ. For the optical bands we adopt the QSO template spectrum described in § 3.

These SEDs (describing the emission of a type 1 AGN) must be compared with the *intrinsic* nuclear emission, which in case of absorbed sources could be very different from the observed one. The problem is tackled starting from the X-ray spectral analysis and assuming the picture proposed by the unified model:

1. X-ray emission:

(*a*) We *de-absorb* the X-ray flux, adopting for the CDF-S sources the intrinsic $N_{\rm H}$ quoted by Tozzi et al. (2006); since the analysis of CDF-N X-ray emission (Alexander et al. 2003) does not include an intrinsic absorption, we derive it from the hardness ratios and redshifts, assuming a mean photon index $\Gamma = 1.8$. As shown in Table 5, only one object of the sample exhibits a hydrogen column density $N_{\rm H} \simeq 1.5\times10^{24}$ cm^{-2} (Compton-thick candidate).

(*b*) We recover the *intrinsic* X-ray luminosity normalizing a power-law spectrum having the same X-ray photon index of the source (for the CDF-S) or with Γ fixed to 1.8 (for the CDF-N) so that it matches the intrinsic X-ray flux.

2. Optical bands:

(*a*) We compare the QSO template spectrum with the optical nuclear magnitudes, computing

$$\chi^2 = \sum_{j=1}^{N_{\rm bands}} \left[\frac{F_{{\rm obs},j} - b\times F_{{\rm templ},j}}{\sigma_j}\right]^2,$$

where b is a normalization constant, while $F_{{\rm obs},j}$, $F_{{\rm templ},j}$, and σ_j are the observed and template fluxes, and the uncertainty of the former, in the optical band j, respectively.

(*b*) Normalizing the QSO template with the value of b corresponding to the minimum value for χ^2, we obtain the optical contribution to the bolometric luminosity.

(*c*) If $N_{\rm H} > 10^{22}$ cm^{-2} (this is the case of about two-thirds of the analyzed sources), the presence of dust in the central regions could affect seriously our estimate of nuclear magnitudes. In this case, we prefer to ignore the fluxes in *B* and *V* band (where the effects of the absorption are more severe), rather than to assume a quite arbitrary correction factor. So, only the *i* and *z* magnitudes are considered in the fit.

3. Bolometric properties: Connecting the power-law spectrum and the QSO template normalized as described before, we recover the X-ray–to–optical ratio, the bolometric luminosity of the AGN and the hard X-ray bolometric correction.

TABLE 5
Derived Properties

ID (1)	Redshift (2)	N_H (10^{22} cm^{-2}) (3)	log $L_{2-8\,keV}$ (ergs s^{-1}) (4)	log L_{bol} (ergs s^{-1}) (5)	Bulge M_R (mag) (6)	log M_{BH} ($M_\odot$) (7)	log λ (8)
				CDF-N			
114	0.679	0.50	43.29	$44.79^{+0.90}_{-0.85}$	-21.88 ± 0.29	8.25 ± 0.36	-1.57 ± 0.36
141	0.747	2.02	42.49	$43.49^{+0.67}_{-0.59}$	-20.50 ± 0.33	7.56 ± 0.37	-2.19 ± 0.37
150	0.762	8.22	42.89	$43.72^{+0.31}_{-0.22}$	-19.18 ± 0.32	6.90 ± 0.37	-1.29 ± 0.37
	...	...	...	44.36	...	6.60	-0.35
170	0.680	3.37	42.46	$43.37^{+0.31}_{-0.25}$	-20.41 ± 0.29	7.52 ± 0.36	-2.26 ± 0.36
194	0.555	0.00	42.77	$43.23^{+0.24}_{-0.17}$	-18.84 ± 0.24	6.73 ± 0.35	-1.62 ± 0.35
	...	...	...	43.89	...	6.43	-0.65
222	0.857	1.31	43.98	$43.84^{+0.84}_{-0.76}$	-21.30 ± 0.35	7.96 ± 0.37	-2.23 ± 0.37
243	0.961	4.23	42.50	$44.81^{+0.30}_{-0.17}$	-20.97 ± 0.40	7.80 ± 0.39	-1.10 ± 0.39
285	0.955	0.36	43.01	$43.51^{+0.70}_{-0.57}$	-20.70 ± 0.40	7.66 ± 0.39	-2.26 ± 0.39
303	0.678	0.17	43.43	$44.02^{+0.74}_{-0.67}$	-21.28 ± 0.28	7.95 ± 0.36	-2.04 ± 0.36
323	0.514	1.28	43.06	$44.63^{+0.62}_{-0.56}$	-21.78 ± 0.20	8.20 ± 0.34	$-1.68^{+0.34}_{-0.35}$
368	0.935	1.15	42.65	$43.65^{+0.31}_{-0.17}$	-19.67 ± 0.41	7.14 ± 0.39	-1.61 ± 0.39
404	0.978	16.63	42.66	$44.10^{+0.53}_{-0.36}$	-21.38 ± 0.40	8.00 ± 0.39	-2.01 ± 0.39
412	0.474	3.68	42.46	$43.50^{+0.32}_{-0.29}$	-15.98 ± 0.25	5.30 ± 0.35	$+0.09 \pm 0.35$
439	0.839	0.22	42.20	$44.25^{+0.90}_{-0.84}$	-21.83 ± 0.35	8.22 ± 0.37	-2.08 ± 0.37
451	0.838	0.57	42.33	$43.63^{+0.35}_{-0.30}$	-21.77 ± 0.35	8.19 ± 0.37	-2.68 ± 0.38
				CDF-S			
34	0.839	0.64	43.04	$44.10^{+0.37}_{-0.39}$	-20.28 ± 0.35	7.45 ± 0.37	-1.46 ± 0.37
40	0.668	5.56	43.15	$44.14^{+0.42}_{-0.43}$	-20.59 ± 0.29	7.60 ± 0.36	-1.58 ± 0.36
42	0.734	0.19	44.22	$45.78^{+0.24}_{-0.13}$	-18.39 ± 0.33	6.50 ± 0.37	$+1.16 \pm 0.37$
	...	...	...	45.78	...	7.86	-0.19
44	0.734	1.75	42.86	$44.00^{+0.45}_{-0.52}$	-20.03 ± 0.32	7.32 ± 0.37	-1.44 ± 0.37
47	0.733	7.99	43.01	$44.15^{+0.30}_{-0.31}$	-20.48 ± 0.32	7.55 ± 0.37	-1.51 ± 0.37
48	0.534	0.13	42.58	$43.75^{+0.34}_{-0.31}$	-20.99 ± 0.24	7.81 ± 0.35	-2.17 ± 0.35
51	0.670	1.75	42.41	$43.39^{+0.23}_{-0.30}$	-18.12 ± 0.34	6.37 ± 0.37	-1.09 ± 0.37
52	0.569	0.04	42.92	$44.11^{+0.25}_{-0.19}$	-19.38 ± 0.25	7.00 ± 0.35	-1.01 ± 0.35
151	0.604	23.16	43.07	$43.90^{+0.28}_{-0.25}$	-19.81 ± 0.25	7.22 ± 0.35	-1.43 ± 0.35
	...	...	...	44.47	...	6.92	-0.56
156	0.545	3.59	42.27	$43.23^{+0.23}_{-0.46}$	-20.15 ± 0.23	7.39 ± 0.35	-2.27 ± 0.35
170	0.664	1.39	42.10	$43.28^{+0.29}_{-0.44}$	-22.29 ± 0.30	8.45 ± 0.36	-3.29 ± 0.36
	...	...	...	43.27	...	8.15	...
189	0.734	4.40	42.15	$43.27^{+0.30}_{-0.61}$	-20.02 ± 0.33	7.32 ± 0.37	-2.16 ± 0.37
192	0.735	12.55	43.00	$43.95^{+0.24}_{-0.28}$	-20.61 ± 0.32	7.61 ± 0.37	-1.78 ± 0.37
201	0.679	2.63	42.59	$44.00^{+0.25}_{-0.29}$	-14.85 ± 0.40	4.74 ± 0.38	$+1.15^{+0.38}_{-0.39}$
	...	...	...	43.95	...	5.88	-0.05
252	0.481	73.51	42.95	$43.99^{+0.24}_{-0.27}$	-16.78 ± 0.21	5.70 ± 0.35	$+0.18^{+0.35}_{-0.36}$
257	0.549	150.00	43.50	$44.50^{+0.23}_{-0.22}$	-18.62 ± 0.25	6.62 ± 0.35	-0.24 ± 0.35
	...	...	...	44.66	...	6.31	$+0.23$
266	0.735	88.76	43.31	$44.24^{+0.38}_{-0.37}$	-20.45 ± 0.33	7.53 ± 0.37	-1.41 ± 0.37
	...	...	...	44.83	...	7.23	-0.51
511	0.668	0.00	41.81	$43.47^{+0.29}_{-0.44}$	-20.61 ± 0.30	7.62 ± 0.36	$-2.26^{+0.42}_{-0.36}$
613	0.910	37.62	43.34	$44.21^{+0.61}_{-0.22}$	-20.87 ± 0.14	7.74 ± 0.34	$-1.65^{+0.36}_{-0.35}$

Notes.—Col. (1): source number, as in Table 1; col. (2): redshift for the optical counterpart, as in Table 1; col. (3): X-ray absorption, from Tozzi et al. (2006) for the CDF-S, and as recovered from the hardness ratios reported in Alexander et al. (2003), assuming $\Gamma = 1.8$ for the CDF-N; col. (4): unabsorbed X-ray luminosity in the 2–8 keV band; col. (5): bolometric luminosity, recovered as described in § 4.2; col. (6): absolute magnitude of the bulge component in the *R* band rest-frame corrected for passive evolution (see § 4.1); col. (7): mass of the central BH, computed from eq. (1); col. (8): Eddington ratio, defined as $\lambda = L_{bol}$ (ergs s^{-1})/($1.3 \times 10^{38} M_{BH}$ [$M_\odot$]). In the case of nucleus-dominated or host-dominated sources (according to the criteria established in § 3.1), the second line shows the parameters obtained starting from the upper limits to the optical magnitudes determined as discussed in the same section.

We remind the reader that the mid-IR fluxes detected by *Spitzer* for 18 of the southern objects analyzed are well explained by the expected contribution from the dusty torus around the nucleus (see the left panel of Fig. 4*b* for the representative source, and the corresponding figure in the electronic edition for the others). On the other hand, the torus emission is just the reradiation of a fraction of the "isotropic" radiation from the very nuclear region (see, e.g., Granato & Danese 1994). So, the IR emission from the putative torus should not be included in the budget of bolometric emission for type 1 AGNs and even for type 2 AGNs, when correction for absorption is done at shorter wavelengths, as in our case. The right panel of Figure 4*b* shows the result of the fit in the generic case, the source CDF-S ID 34 ($z = 0.839$); fits for the other sources are shown in the electronic edition.

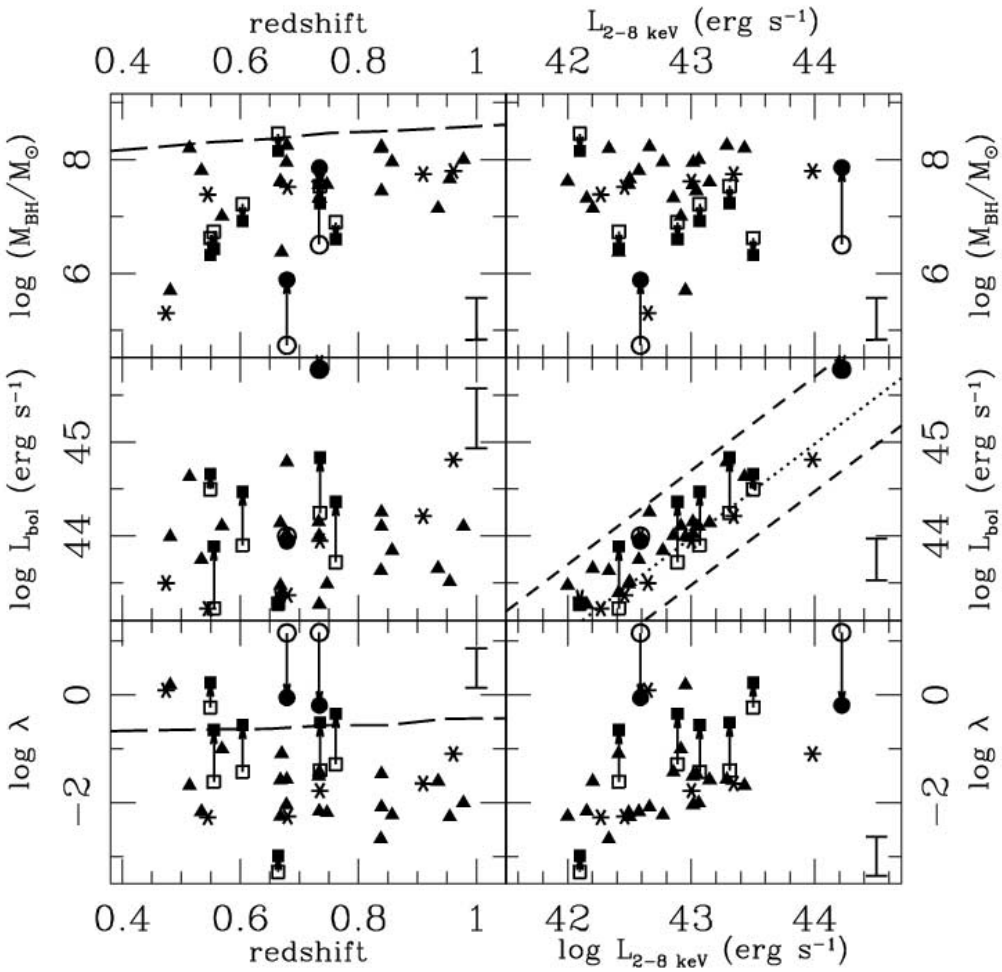

FIG. 6.—BH masses (*top panels*), bolometric luminosities (*middle panels*), and Eddington ratios (*bottom panels*) vs. redshift (*left panels*) and unabsorbed hard X-ray luminosity (*right panels*) for the analyzed sample. Triangles indicate sources for which we are confident that the results from the morphological decomposition are reliable. For nucleus-dominated or host-dominated sources (according to the criteria established in § 3.1), filled circles and squares mark the upper limits to M_{BH} and L_{bol}, respectively; open symbols mark the values obtained from the decomposition. Stars emphasize the cases in which we find low X-ray bolometric correction, $L_{bol}/L_X < 10$; the dotted line in the plot of bolometric luminosities vs. hard X-ray luminosities represents this threshold, while the dashed lines correspond to the "extreme" values for the X-ray bolometric correction reported in § 5. Only mean error bars are reported to avoid clutter. For the distribution of L_{bol} vs. L_X (*middle right panel*), we plot the component of the error on L_{bol} that is independent from the error on L_X. As a comparison, we overplot to our distribution of masses and Eddington ratios versus redshift the mean (within $\Delta z = 0.1$ bins) values found by McLure & Dunlop (2004) for their full SDSS quasar sample (*long-dashed line*). [*See the electronic edition of the Journal for a color version of this figure.*]

We identify two possible sources of uncertainty in our estimate of the bolometric luminosity:

1. A systematic error induced by the selection of one spectral shape common to all the sources for the optical emission: for each source, starting from a spectral shape $f_\lambda \propto \lambda^\alpha$ we determine the scatter in the optical luminosity due to a different choice in the slope ($\alpha = -1.37 \pm 0.25$, as recovered by Fontanot et al. [2006] by averaging out the rest-frame spectra of 215 SDSS QSO). The scatter, calculated assuming as a pivot the flux at the frequency corresponding to the *i*-band wavelength in the observed frame, results to be of the order of $\Delta \log L = 0.2$.
2. The uncertainties associated with the decomposed magnitudes propagate on to the best-fit normalization of the QSO template: for each source we repeat the fit changing the normalization of the template until $\Delta\chi^2 = 1$.

Bolometric luminosities with the estimated errors are shown in Table 5. Their dependence on redshift and hard X-ray luminosity is shown in Figure 6 (*middle panels*). In host-dominated objects the nuclear flux provided by the decomposition could be underestimated. For these six sources, the same procedure has been applied also assuming as nuclear magnitudes the upper limits recovered as described in § 3.1. The corresponding upper limit to L_{bol} is reported as a second line in Table 5. While the upper limits of their optical nuclear luminosity may be a factor up to 200 larger than the decomposed ones, the bolometric upper limit is larger by factor of 10, at most. We find bolometric luminosities in the range $10^{43} \leq L_{bol} \leq 10^{45}$ ergs s^{-1}, with only one exception (the source CDF-S ID 42, $L_{bol} \simeq 5.9 \times 10^{45}$ ergs s^{-1}). The X-ray–to–optical ratios and the hard X-ray bolometric corrections span the range between -1.4 and -0.9, and between 6.8 and 46.7, respectively.

5. DISCUSSION

The analysis presented in the previous sections highlights some interesting properties of this sample of X-ray-selected AGNs:

1. In several objects the nuclear optical luminosity is very low and, correspondingly, the estimated spectral index $\alpha_{ox} = \log (L_{\nu[2500\ \text{Å}]}/L_{\nu[1\ \text{keV}]})/\log (\nu[2500\ \text{Å}]/\nu\,[1\ \text{keV}])$ (see Zamorani et al. 1981) is large. In the top panel of Figure 7 we report the distribution of spectral indices recovered from the decomposition (*solid line*; the mean value for the error on α_{ox} is 0.05). In particular we obtain $\langle \alpha_{ox} \rangle \simeq -1.1$, compared to the median $\alpha_{ox} = -1.51$ found for a sample of SDSS AGNs by Strateva et al. (2005) (Fig. 7,

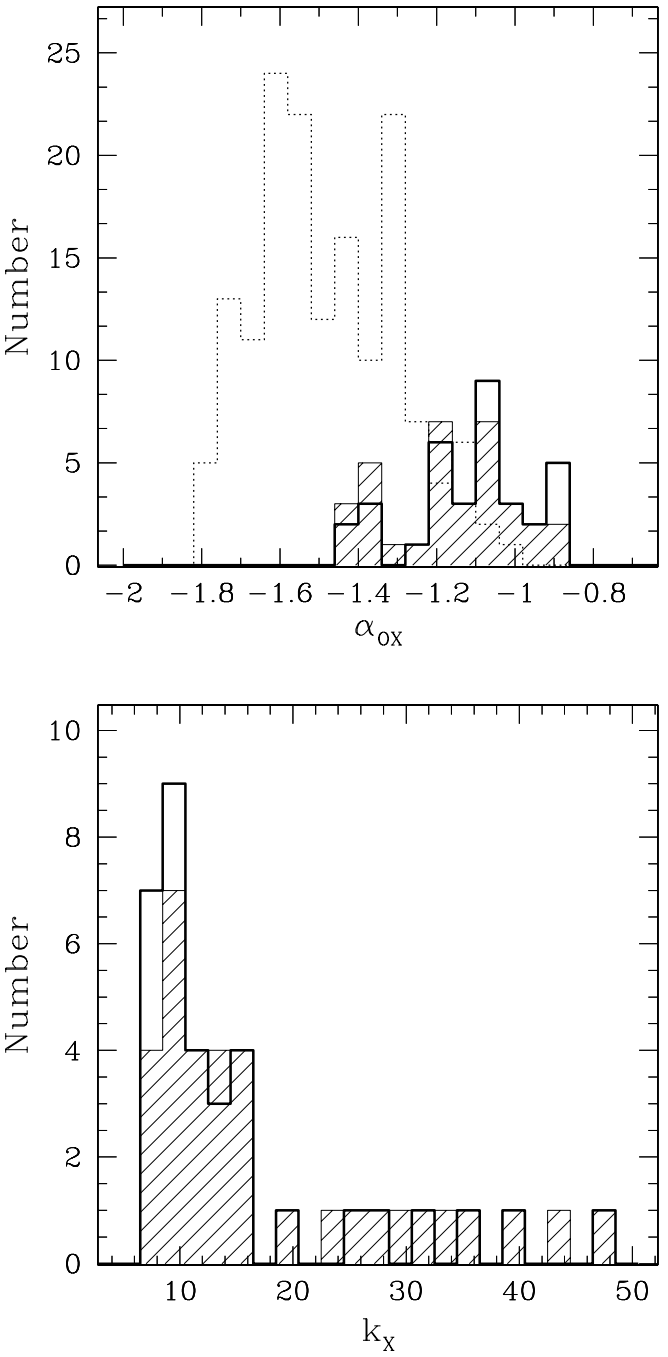

FIG. 7.—Distribution in spectral indices α_{ox} (*top panel*) and X-ray bolometric corrections k_X (*bottom panel*) of the analyzed sample; hatched areas show the same distributions as after the check against nucleus-dominated or bulge-dominated sources (see § 3.1). The dotted line in the spectral index distribution refers to the values found by Strateva et al. (2005) for the X-ray-detected sources in their "main" SDSS sample (155 objects with $0.1 \lesssim z \lesssim 4.5$).

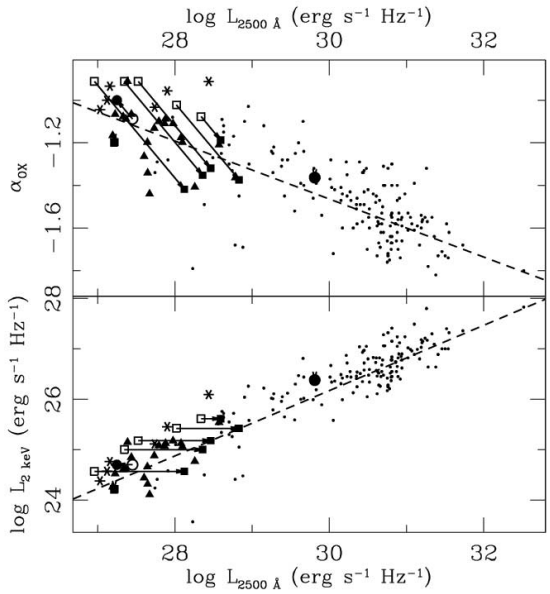

FIG. 8.—Dependence on the 2500 Å monochromatic luminosity of α_{ox} (*top panel*) and $L_{2\ keV}$ (*bottom panel*). Symbols without arrows indicate sources for which we are confident that the results from the morphological decomposition are reliable (according to the criteria established in § 3.1); arrows mark how nucleus-dominated (*circles*) or host-dominated (*squares*) sources move in the plane from the value derived from the decomposition (*open symbols*) to that obtained considering the upper limits to M_{BH} and L_{bol} (*filled symbols*), respectively. Stars indicate the cases in which we find low X-ray bolometric correction, $L_{bol}/L_X < 10$. Dots mark data from Strateva et al. (2005) for the X-ray-detected sources in their "main" SDSS sample (155 objects with $0.1 \lesssim z \lesssim 4.5$); dashed lines are the best–fit linear relations for their combined sample: $\alpha_{ox} = -0.136 \log L_{2500\ Å} + 2.616$ (*top panel*) and $\log L_{2\ keV} = 0.648 \log L_{2500\ Å} + 6.734$ (*bottom panel*). [*See the electronic edition of the Journal for a color version of this figure.*]

dotted line in top panel). Even including for the host-dominated sources the α_{ox} obtained assuming the upper limits to the optical emission, the mean spectral index does not change much, $\langle \alpha_{ox} \rangle \simeq -1.2$ (the distribution is shown as hatched area in the top panel of Fig. 7), reinforcing the claim that our selection picked out sources rather different from the SDSS sample. We may expect that the X-ray selection at very low flux limits singles out objects exhibiting α_{ox} lying in the distribution at the opposite side with respect to the values found for optically selected QSOs. Strateva et al. (2005) found evidence of an increase of the hard X-ray–to–optical luminosity ratio with decreasing optical luminosity (see their Fig. 11). It is worth noting that the average value of the spectral index of our sample falls on the extrapolation of the correlation between X-ray and UV emission found by Vignali et al. (2003) for optically selected QSOs and confirmed by Strateva et al. (2005). In Figure 8 we compare our results with their data (see the caption for an explanation of the symbols). Thus the trend of increasing the X-ray–to–UV luminosity ratio with decreasing UV luminosity is confirmed down to very low luminosity $L_{2500\ Å} \sim 10^{27}$ ergs s^{-1} Hz^{-1}.

2. The bolometric–to–X-ray luminosity ratio, i.e., the X-ray bolometric correction k_X, turns out to be generally small. Its distribution is peaked around $k_X \simeq 10$, with a tail extending to $k_X \simeq 50$, a median value $k_X \simeq 12$, and a mean error of 0.5 (see the bottom panel in Fig. 7; the hatched area marks the distribution after the correction applied for host-dominated sources). In particular, objects with low k_X could be the analogs of X-ray AGNs found in optically normal galaxies (e.g., the so-called XBONGs; see Comastri et al. 2002; Severgnini et al. 2003; Brusa et al. 2003). We can compare the distribution of k_X in our low-luminosity X-ray-selected AGNs with bolometric corrections reported in literature for different samples of AGNs, first of all the sample of optically bright quasars studied by Elvis et al. (1994). If we remove the IR contribution (i.e., nuclear emission reradiated by the circumnuclear torus) from their observed bolometric luminosities, the median bolometric correction is $k_X \simeq 25$. Note that in this sample of QSOs the emission in the 0.1–1 μm range of wavelengths yields on average about 30% of the bolometric luminosity, while in our sample the percentage is lower, about 8%. The

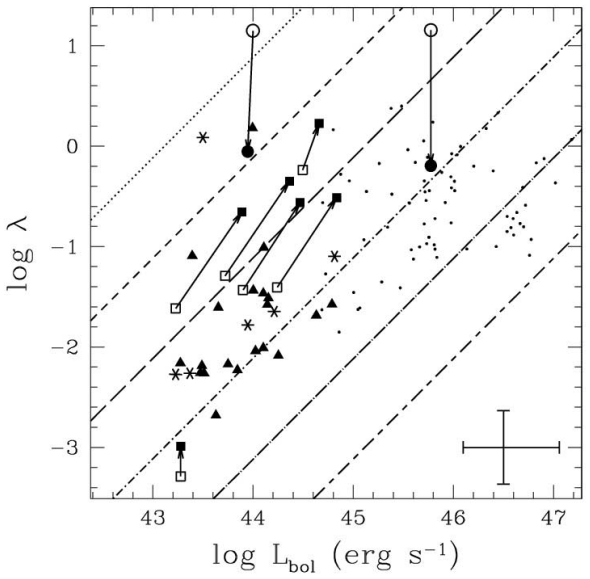

FIG. 9.—Eddington ratios as function of bolometric luminosities for the analyzed sample and for the PG QSO sample studied by Vestergaard & Peterson (2006) marked with dots. Triangles indicate sources for which we are confident that the results from the morphological decomposition are reliable. For nucleus-dominated or host-dominated sources (according to the criteria established in § 3.1), filled circles and squares mark the upper limits to $M_{\rm BH}$ and $L_{\rm bol}$, respectively; open symbols mark the values obtained from the decomposition. Stars emphasize the cases in which we find low X-ray bolometric correction, $L_{\rm bol}/L_{\rm X} < 10$; the error bars reported represent the mean uncertainties in the derived quantities. From top to bottom, the lines define the trend for BH masses of $10^5\ M_\odot$ (*dotted line*), $10^6\ M_\odot$ (*dashed line*), $10^7\ M_\odot$ (*long-dashed line*), $10^8\ M_\odot$ (*dot-dashed line*), $10^9\ M_\odot$ (*dot-long-dashed line*), and $10^{10}\ M_\odot$ (*short-dash–long-dashed line*), respectively. [*See the electronic edition of the Journal for a color version of this figure.*]

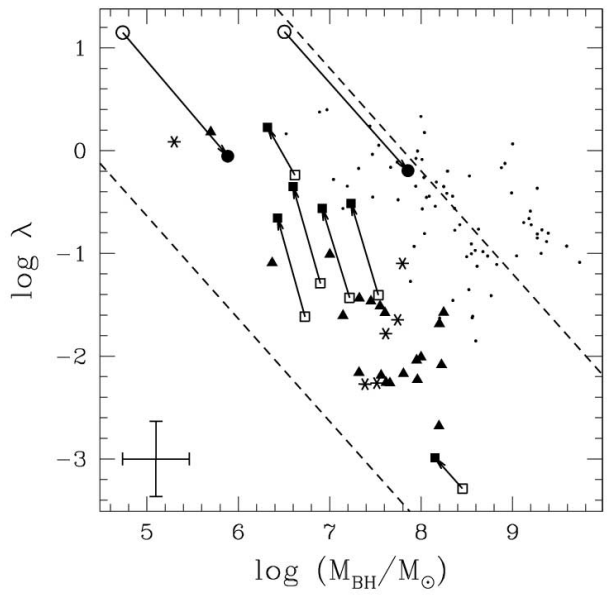

FIG. 10.—BH masses vs. Eddington ratios for the analyzed sample. Symbols without arrows refer to sources for which we are confident that the results from the morphological decomposition are reliable. Arrows mark how sources nucleus-dominated (*circles*) and host-dominated (*squares*) move in the plot from the value derived from the decomposition (*open symbols*) to that corrected as described in § 3.1. Stars emphasize the cases in which we find low X-ray bolometric correction. The error bars reported represent the mean uncertainties in the derived quantities. The dashed lines define the region in the plane in which the sources are confined on the base of the hard X-ray luminosity range sampled (*bottom line:* $L_{2\text{–}8\,\rm keV} = 10^{42}$ ergs s^{-1}; *top line:* $L_{2\text{–}8\,\rm keV} = 1.7 \times 10^{44}$ ergs s^{-1}, the highest value in our sample) and assuming two bracketing values for the X-ray bolometric correction ($k_{\rm X,\,min} = 3$ and $k_{\rm X\,max} = 50$, respectively). Dots mark data from Vestergaard & Peterson (2006) for PG QSOs at redshift $z \leq 0.4$. [*See the electronic edition of the Journal for a color version of this figure.*]

same analysis applied to the sample of type 1 AGNs listed by Kuraszkiewicz et al. (2003) yields a median $k_{\rm X} \simeq 18$ with a maximum value $k_{\rm X} \simeq 60$ for AGNs with $10^{43} \leq L_{2\text{–}10\,\rm keV} \leq 10^{46}$ ergs s^{-1}. X-ray bolometric corrections in the range $k_{\rm X} \simeq 12$–18 have been derived for low-luminosity type 1 AGNs by Fabian (2004). Our results suggest that the average bolometric correction for the X-ray emission $k_{\rm X}$ might be a decreasing function of the X-ray luminosity, as indicated also by Shankar et al. (2004) and Marconi et al. (2004).

3. For our sample the Eddington ratios, $\lambda = L_{\rm bol}({\rm ergs\ s^{-1}})/(1.3 \times 10^{38} M_{\rm BH}\ [M_\odot])$, do not exhibit any significant correlation with either redshift or X-ray luminosity (Fig. 6, *bottom panels*). In general, we find rather low Eddington ratios. This is an inevitable consequence of finding AGNs of very low luminosity (all but one in our sample exhibit $10^{43} \leq L_{\rm bol} \leq 10^{45}$ ergs s^{-1}) in galaxies with large bulge component. We plot in Figure 9 the Eddington ratios as function of bolometric luminosities for our sample and for the PG QSO sample studied by Vestergaard & Peterson (2006). The authors derived BH masses and bolometric luminosities for a large fraction of PG QSOs at redshift $z \leq 0.4$, by exploiting the most recent calibration of the BH mass as function of the Hβ broadband luminosity and FWHM. The behavior of the PG QSO sample is quite similar to that found for QSOs at higher redshift. For instance, Kollmeier et al. (2006) found Eddington ratios in the range $0.1 \leq \lambda \leq 1$ for a sample of powerful AGNs covering the redshift range $z \sim 0.3$–4, and Warner et al. (2004) estimated that 27% of their QSO sample ($0 \leq z \leq 5$) exhibits $\lambda \geq 1$. The two samples compared in Figure 9 are probing different, but complementary, ranges of bolometric luminosity and redshift. It is apparent that the low-luminosity sample contains a large fraction of AGNs with quite small Eddington ratio. The small number of objects with large $L_{\rm bol}$ and small λ is related to the empirical limit to the BH mass, which cannot exceed several thousandths the mass of the stars in the host galaxy (see, e.g., Magorrian et al. 1998; Gebhardt et al. 2000; see Ferrarese et al. 2006 for a recent discussion). In fact, large bolometric luminosities ($L_{\rm bol} \geq 10^{47}$ ergs s^{-1}) would obviously be easy to observe; but coupled with small Eddington ratios ($\lambda \leq 10^{-1}$), they would imply BH masses $M_{\rm BH} \geq 10^{10}\ M_\odot$, as apparent in Figure 9. These masses would be larger than several percent of the mass in stars of the largest galaxies ($M \leq 10^{12}\ M_\odot$).

On the other hand, our sample contains galaxies with large halos and, therefore, large central BH masses, hosting low-luminosity AGNs radiating at largely sub-Eddington regime. In Figure 10 we report the estimate of the Eddington ratio as a function of the BH mass for our sample and for the PG QSOs of Vestergaard & Peterson (2006). Woo & Urry (2002) noted that in their compilation there was no object with $L_{\rm bol} \leq 10^{44}$ ergs s^{-1} and $\lambda \gtrsim 1$. This deficit was ascribed by these authors to difficulty in selecting such AGNs due to dilution by host galaxy light. On the other hand, our selection is designed to set up a fair sample of low-luminosity AGNs. Indeed, as a result, we find in our sample a few AGNs with $L_{\rm bol} \leq 10^{45}$ ergs s^{-1} and $\lambda \sim 1$. Finally, the tail of the nuclear X-ray emission ($10^{41} \leq L_{2\text{–}10\,\rm keV} \leq 10^{42}$ ergs s^{-1}) at very low Eddington ratios, $\lambda \lesssim 10^{-3}$, in a redshift interval very similar to ours, $0.3 < z < 0.9$, has been detected by Brand et al. (2005) with the stacking technique applied to a sample of red galaxies (i.e., galaxies with significant bulge and, by implication,

large central BH). On the basis of our data and of the results of other authors (Woo & Urry 2002; McLure & Dunlop 2004; Warner et al. 2004; Kollmeier et al. 2006; Vestergaard & Peterson 2006), we can conclude that low-luminosity objects ($L_{bol} \lesssim 10^{44}$ ergs s^{-1}) exhibit a large range of values of Eddington ratio ($10^{-3} \lesssim \lambda \lesssim 1$), while at high luminosity ($L_{bol} \gtrsim 10^{46}$ ergs s^{-1}) the range is limited to $10^{-1} \lesssim \lambda \lesssim$ a few. The result can also be represented as a decline of the average value of the Eddington ratio with decreasing bolometric luminosity. This behavior coupled with the shift of AGN luminosity function toward lower luminosity since $z \simeq 2.5$, may mimic a decrease of the Eddington ratio with decreasing redshift (see, e.g., McLure & Dunlop 2004; Vestergaard 2004; Volonteri et al. 2006). It is worth noting that Salucci et al. (1999), Marconi et al. (2004), and Shankar et al. (2004) have shown that a dependence of λ on luminosity and/or on redshift is required in order to match the local BH mass function to the mass function estimated from the evolution of the luminosity function of the AGNs.

4. A remarkable feature of the studied sample is the small number of AGNs with mass $M_{BH} \lesssim 10^6\ M_\odot$ *emitting at Eddington ratio* $\lambda \sim 1$, which are expected to show up at this redshift and luminosity range. We stress here that X-ray surveys at faint limits are very efficient in selecting these low-luminosity AGNs, because of the maximum contrast with the host galaxy. Therefore, we do not expect that the CDF-N and CDF-S X-ray surveys are missing objects at least up to $z \simeq 1$ (unless they are extremely absorbed, with $N_H > 10^{23}$ cm^{-2}; see Fig. 14 in Tozzi et al. 2006). The X-ray sources lying in the GOODS fields have been optically identified practically at 100% level (see Table A1, col. [4]). Selecting only "isolated" objects without companions within a radius of 2″ decreases our sample from 53 to 34 objects (see Table A1, cols. [11], [12], [13], and [14] of Table A1). Keeping this radius constant, we are in fact increasing the physical radius with the redshift. The increasing number of non "isolated" objects with redshift is the consequence of this choice and of the possible increase of really interacting galaxies. On the other hand, since the host luminosity distribution of pairs in active and normal samples does not show statistically significant differences, and does not differ dramatically from that of isolated galaxies (Virani et al. 2000; Bergvall et al. 2003), we do not expect that the excluded objects would alter our conclusion. Nevertheless, we caution that our conclusion on the dearth of objects with low BH mass and with accretion rate near the Eddington limit is solid in the range of redshift $0.4 < z < 0.8$. It is worth recalling here that the BH masses reported in Figures 6 and 10 have been estimated, following McLure & Dunlop (2002), through equation (1), which yields values a factor about 1.5–2 lower than those evaluated through the M_{bulge}-M_{BH} relations proposed by Kormendy & Gebhardt (2001) and Marconi & Hunt (2003). If the scarcity is real, a possible explanation is that the bulk of the mass is accreting on smaller SMBHs at high redshift, when the stellar bulge is also built up. Later, both large and small SMBHs are on average accreting at low rates. In this case the $\lambda \sim 1$ accretion phase occurs at $z \geq 1$, outside the limit of our primary selection. In addition to that, the lack of small SMBHs can mirror a significant decrease in number density of BHs with $M_{BH} \leq 10^6\ M_\odot$. Shankar et al. (2005) found a fall-off of the ratio between BH and halo mass at $M_{BH} \leq 5 \times 10^6\ M_\odot$, by comparing their respective mass functions. It is worth noting that this behavior is predicted in models of galaxy and AGN formation, in which the BH grows in parallel with the old stellar bulge component and the stellar and AGN feedback affects the efficiency of the gas to cool and form stars (Granato et al. 2001; Granato et al. 2004).

Our analysis reveals that most of the low-luminosity X-ray-selected AGNs in the explored redshift and luminosity intervals are powered by massive BHs $M_{BH} \geq 3 \times 10^6\ M_\odot$ and, as a consequence, that we are mostly witnessing a renewal at low-level activity, in galaxies with only small amount of cold gas in the central regions. Probably, most of the BH mass that we typically find in objects of our sample has been accreted during a higher luminosity phase. Sporadic activity at low accretion rate has been also observed in EROs at $z < 2$ (Brusa et al. 2005). It is very likely that short and sporadic activity is the rule for the SMBHs after the bright QSOs phase. Although the inferred low Eddington ratios can be even sustained for significant time intervals by a number of galactic processes, minor mergers, and/or instabilities in the host galaxy induced by satellites are often invoked (see, e.g., Cavaliere & Vittorini 2002). On the other hand, Waskett et al. (2005) claim that the environment of a sample of low-luminosity hard X-ray-selected AGNs is the same of normal inactive galaxies in the same range of redshift and with similar optical properties. Moreover, recent attempts to find statistical evidence of recent merging in AGN host galaxies at $z \sim 0.4$–1.3 are negative (Grogin et al. 2005).

6. CONCLUSIONS

We have presented the results of a morphological and photometric analysis of a sample of X-ray-selected AGNs in the GOODS fields with redshifts between 0.4 and 1. The sample is representative of AGNs in the luminosity range $10^{42} \leq L_{2-8\,keV} \leq 5 \times 10^{43}$, which are responsible for a large fraction of the XRBs in the selected redshift range (see, e.g., Ueda et al. 2003). The imaging capability of *HST* and the large spectral coverage from *B* to *z* bands allowed for an accurate separation of the bulge and nuclear luminosity for the 34 objects in our sample.

The bolometric luminosity has been computed for each AGN by linking with standard templates the intrinsic X-ray luminosity and the nuclear luminosity in the UV and optical bands. We estimated the central BH mass from the bulge luminosity, under the assumption that their relationship observed in the local Universe is already in place since $z \sim 1$. We do not find any significant correlation of X-ray luminosities with either BH masses or Eddington ratios.

The main findings of this work are the following.

1. As expected, this X-ray-selected sample is characterized by a high ratio of X-ray–to–optical nuclear luminosity with respect to the values found for optically selected AGNs; we confirm the increase of this ratio with decreasing UV luminosity down to $L_{2500\ Å} \sim 10^{27}$ ergs s^{-1} Hz^{-1}.

2. By comparing the X-ray bolometric corrections in our low-luminosity AGNs with that of bright QSOs, we obtain a trend of decreasing the X-ray bolometric correction factor k_X with the luminosity.

3. We find rather low Eddington ratios for our low bolometric luminosity sample. A comparison with higher luminosity samples suggests that the scatter in Eddington ratios is increasing with decreasing luminosity. This is a consequence of the expected increase of probability of low Eddington ratios with decreasing bolometric luminosity.

4. The estimated BH masses span a wide range of values; but we do find only $\leq$10% of nuclei with $M_{BH} \leq 10^6\ M_\odot$ emitting near the Eddington limit, at least at redshift $z < 0.8$. This paucity could mirror a decrease in the number density of BHs with $M_{BH} \leq 10^6\ M_\odot$, or indicate that also for these smaller BHs the bulk of the accretion takes place at $z \geq 1$.

Our results strongly suggest that most of the low-luminosity X-ray-selected AGNs at $z \leq 0.8$ are powered by rather massive BHs, experiencing a low-level accretion in a gas-poor environment.

In the future we plan to expand the sample in order to study in detail how the BHs powering low-luminosity AGNs populate the $M_{\rm BH}$-λ plane. We also want to increase the spectroscopic coverage in order to be able to exploit also the virial theorem to estimate the BH mass. The small number of low-mass BHs, $M_{\rm BH} \leq 10^6\,M_{\odot}$, if confirmed and statistically quantified, will be extremely informative on AGN formation and evolution, and on their demography.

We warmly thank M. Dickinson, B. Simmons, and all the GOODS team for enlightening discussions and suggestions that improved this work. We are grateful to A. Bressan for providing us observed spectra of local elliptical galaxies, and to C. Peng for making GALFIT publicly available. L. B. thanks L. Maraschi, R. Della Ceca, V. Braito, and E. Carretta for useful discussions. We warmly thank the referee for carefully reading the manuscript, and for her/his suggestions, which significantly improved the paper. We acknowledge the support of MIUR with the PRIN 2003 and of INAF with the COFIN 2002 "Cosmological evolution of galaxies and their active nuclei." Support for the GOODS *HST* Treasury Program was provided by NASA through grants HST-GO-09425.01-A and HST-GO-09583.01 from the Space Telescope Science Institute, which is operated by the Association of Universities for Research in Astronomy under NASA contract NAS 5-26555.

APPENDIX A

DETAILS ON SAMPLE SELECTION

In this Appendix we describe the steps leading to the selection of the sources forming the sample B; they are summarized in Table A1.

We start selecting from the *Chandra* X-ray catalogs the X-ray sources lying in the two regions of the sky defined by the GOODS ACS South and North catalogs in the *i* band (`h_goods_si_r1.1z_cat.txt` and `h_goods_ni_r1.1z_cat.txt`[12]; col. [3]). By cross-correlating the GOODS optical catalogs with the *Chandra* X-ray catalogs we find an optical counterpart for ~98%–99% among these (col. [4]).

The spectroscopic follow-up of the X-ray survey has been presented by Szokoly et al. (2004) and Barger et al. (2003) for the CDF-S and the CDF-N, respectively. Spectroscopic redshifts are reported for ~48% of the whole CDF-S X-ray sources and ~56% for that of the whole CDF-N. Photometric redshifts are reported by Mobasher et al. (2004), Zheng et al. (2004), Mainieri et al. (2005), and Grazian et al. (2006) for ~99% of X-ray sources in the whole CDF-S, and by Barger et al. (2003) for the whole CDF-N (so the completeness of the redshift determination in the north GOODS field rises to ~80%). Columns (5) and (6) show the number of X-ray sources with optical counterpart in the GOODS catalogs for which there are spectroscopic or photometric redshift information, respectively. As stressed in § 2, this step does not induce any bias against optically faint sources (see also Fig 1).

In the following step we restrict the sample to the redshift range ($0.4 < z < 1$), leading to a substantial decrease in the source number. By comparing columns (5), (6), (7), and (8), it clearly appears that a larger decrease takes place for sources with only photometric redshifts. This result is not surprising, considering the distribution of spectroscopic and photometric redshifts of the sources in the south field (for which the redshift determination is almost complete): the first is clearly peaked between 0.5 and 1.2, while in the second case ~88% of the sources have $z > 1$. Besides, the fraction of sources retained in this step is reassuringly consistent with what estimated by integrating the QSO luminosity function down to the GOODS flux limits. We expect in fact to observe in the redshift range $0.4 < z < 1$ 37% of the total number in the interval $0 < z < 4$, and the fraction of spectroscopic and photometric redshifts assigned to the $0.4 < z < 1$ range turns out to be 27%.

Then, we discard all sources with $L_{2-8\,\rm keV}$ lower than 10^{42} ergs s^{-1}, producing a second substantial reduction in the source number.

As described in Appendix B, we also reject sources for which the quality of one or more cutouts is significantly below average, due typically to a nonideal data acquisition (~20%; see cols. [11] and [12]). The objects remaining after this step compose what we define "sample A." In the final step we discard sources that are found to be "not isolated" according to the operational criterion described in the Appendix B. The resulting sample B includes 64% of the sample A.

[12] Available at ftp://archive.stsci.edu/pub/hlsp/goods/catalog_r1.

TABLE A1
Steps in the Sample Selection

				With z Information		$0.4 < z < 1$		$\log L_{\rm X} > 42$		Cutouts OK		Isolates	
Field (1)	Total X-Ray Source (2)	In GOODS Area (3)	With ID GOODS (4)	$z_{\rm spec}$ (5)	$z_{\rm phot}$ (6)	$z_{\rm spec}$ (7)	$z_{\rm phot}$ (8)	$z_{\rm spec}$ (9)	$z_{\rm phot}$ (10)	$z_{\rm spec}$ (11)	$z_{\rm phot}$ (12)	$z_{\rm spec}$ (13)	$z_{\rm phot}$ (14)
CDF-N.....	503	261	258	163	41	93	9	26	5	25	3	15	0
CDF-S	326	197	196	134	60	63	5	32	3	23	2	18	1

Notes.—Col. (1): field observed; col. (2): number of X-ray sources; col. (3): number of X-ray sources in the GOODS area as identified by *i*-band observations; col. (4): number of X-ray sources with optical counterpart in the *i*-band GOODS ACS catalog; cols. (5) and (6): number of X-ray sources identified in the *i*-band GOODS ACS catalog with redshift (spectroscopic, from Barger et al. 2003 and Szokoly et al. 2004; or photometric, from Barger et al. 2003, Grazian et al. 2006, and Zheng et al. 2004); cols. (7) and (8): number of X-ray sources with GOODS counterpart and redshift (spectroscopic or photometric, respectively) between 0.4 and 1; cols. (9) and (10): number of X-ray sources with GOODS counterpart, $0.4 < z < 1$ (spectroscopic or photometric, respectively), and $L_{2-8\,\rm keV} > 10^{42}$ ergs s^{-1}; cols. (11) and (12): number of X-ray sources with GOODS counterpart, $0.4 < z < 1$ (spectroscopic or photometric, respectively), $L_{2-8\,\rm keV} > 10^{42}$ ergs s^{-1}, and without damaged cutouts (sample A); cols. (13) and (14): number of *isolated* X-ray sources with GOODS counterpart, $0.4 < z < 1$ (spectroscopic or photometric, respectively), $L_{2-8\,\rm keV} > 10^{42}$ ergs s^{-1}, and without damaged cutouts (sample B).

APPENDIX B

TWO-DIMENSIONAL PHOTOMETRIC DECOMPOSITION

In this Appendix we present details on the morphological analysis carried out on GOODS ACS images for the 34 sources listed in Table 1. In order to disentangle the main galactic components (nucleus, bulge, and disk), we performed a two-dimensional image decomposition, taking advantage of images in four different passbands. In our analysis we assume a galaxy model composed of a bulge (described by a de Vaucouleur model) and a disk (modeled with an exponential function). Moreover, we always assume the presence of a nuclear source, obtained by adding a point-spread function (PSF) component to the above model. We also assume that, for each component, position angle, axial ratio and optical radius are the same for each passband.

To make the fit we use GALFIT (Peng et al. 2002), a two-dimensional image decomposition program designed to accurately model galaxy profiles and to extract nuclear point sources, combining simultaneously an arbitrary number of profiles. The fitting algorithm constructs a model image, convolves it with a PSF, and finally compares the result with the data. During the fit, the reduced χ^2 is minimized using a Levenberg-Marquardt algorithm (Press et al. 1997). The uncertainties as a function of the pixel position used to calculate the reduced χ^2 are the Poisson errors, and are generated on the basis of the GAIN and the READ-NOISE parameters, recovered using the Weight Map Images provided by the GOODS Team. Finally, in order to construct our own PSF for each band, we have identified in the GOODS ACS images a number of point sources and have averaged them.

The initial guesses for the parameters (magnitudes, scale length, position angle, and semiminor axis to semimajor axis ratio) are drawn from the GOODS ACS public catalog (see footnote 12). In particular, magnitudes reported in this catalog refer to the whole galaxy, while GALFIT requires an initial value for each component: as a starting point, we split the observed value ascribing the same flux to each component. The decomposition has been carried out in a three-step analysis (with a number of free parameters different from step to step); a schematic diagram representing the whole process of analysis is shown in Figure 11.

1. The galaxy is first modeled as pure disk + nucleus in the *B* and *V* filters, with a two-component independent fit, while we assume for the *i* and *z* bands a pure bulge + nucleus description. By comparing the results of the four bands we find a first indication about the position angle (P.A.) and the axis ratio (*b*/*a*) for both the disk and bulge components, and new guesses for the centers and the radii.
2. Morphological parameters are refined assuming the three components (nucleus, bulge, and disk) in all the bands:

(*a*) Centers and radii found during the first step are introduced as new guesses. The centers of the three components are constrained to differ at most by ± 0.1 pixel.
(*b*) If the P.A. is not well determined in the previous step, we rerun GALFIT, constraining the disk P.A. to be within ± 2 deg of the bulge parameter.
(*c*) We fix P.A. and *b*/*a* to the values obtained in the previous run of GALFIT or in the first step.

3. A final run of GALFIT provides the magnitudes associated to each component; centers, radii, P.A., and *b*/*a* are fixed to the values found in the previous step. For each component, they are assumed to be the same in all bands. Only the total fluxes of all components are left free and derived in this last step.

For a number of sources, the quality of one or more ACS images is significantly below average (e.g., due to the source location near the edge of the GOODS field). Because of the number of free parameters, we require the same quality of data in a region of at least 60 pixels. In addition, we require that *all* the four images meet this requirement in order to perform the analysis. We checked that the objects for which these requirements are not satisfied have a random distribution in luminosity, redshift, or spectral classification; so we are confident that rejecting these sources does not introduce any kind of bias against a particular class of objects.

For the same reason mentioned above, objects lying in crowded fields have been excluded from the analysis. As an operational criterion, we reject objects showing a nearby companion within a projected radius of $2''$ (i.e., $\sim$13 kpc at the mean redshift of sources in sample B), without considering if they are really interacting or if it is only a projection effect. In such a way, we discard 19 objects, i.e., 36% of the selected X-ray sources.

Figure 12 shows the distribution in redshift, hard X-ray luminosity, and *i*-band magnitude of the sources rejected for having at least one bad cutout (*thick solid line*) or classified as "not isolated" (following the above definition; *dashed line*), compared with the distributions for the analyzed sources (*thin solid line*; hatched areas show the same distributions for the sources for which we are confident that the results from the morphological decomposition are reliable).

Results of the analysis are reported in Table 2 (magnitudes of bulge, disk, and nucleus) and Table 3 (host galaxy morphological parameters). The errors reported in Table 2 have been evaluated as follows: considering the image in a single filter, we fix all the parameters but the three magnitudes; to determine the range of variability for the magnitude of one component, we increase Δmag in steps of 0.05 and perform a new fit with the two other magnitudes as free parameters until the variation of χ^2 with respect to the best-fit value is $\Delta\chi^2 = 1$ (68% confidence level). For each source, we repeat this procedure for each component in each passband.

A practical way to test the reliability of our estimates is to repeat the analysis using the ACS Ultra Deep Field (UDF; see Beckwith et al. 2003), which is contained in the CDF-S GOODS area. Unfortunately, none of the sources analyzed in the present sample lies inside the region covered by the UDF. We have identified one X-ray source with properties outside but very close to our selection criteria (ID 516, CDF-S; $z = 0.665$, and $L_X = 8.22 \times 10^{41}$ ergs s^{-1}). For this object we have carried out the analysis described above both for the GOODS images and for the UDF data. The photometric differences between the GOODS and UDF analysis turn out to be within the uncertainties estimated in the GALFIT decomposition of the GOODS images (about 0.3 mag). The derived quantities M_{BH} (see § 4.1) and λ (see § 5) differ of $\sim$0.18 dex, consistent with our estimate of the errors (see Table 5).

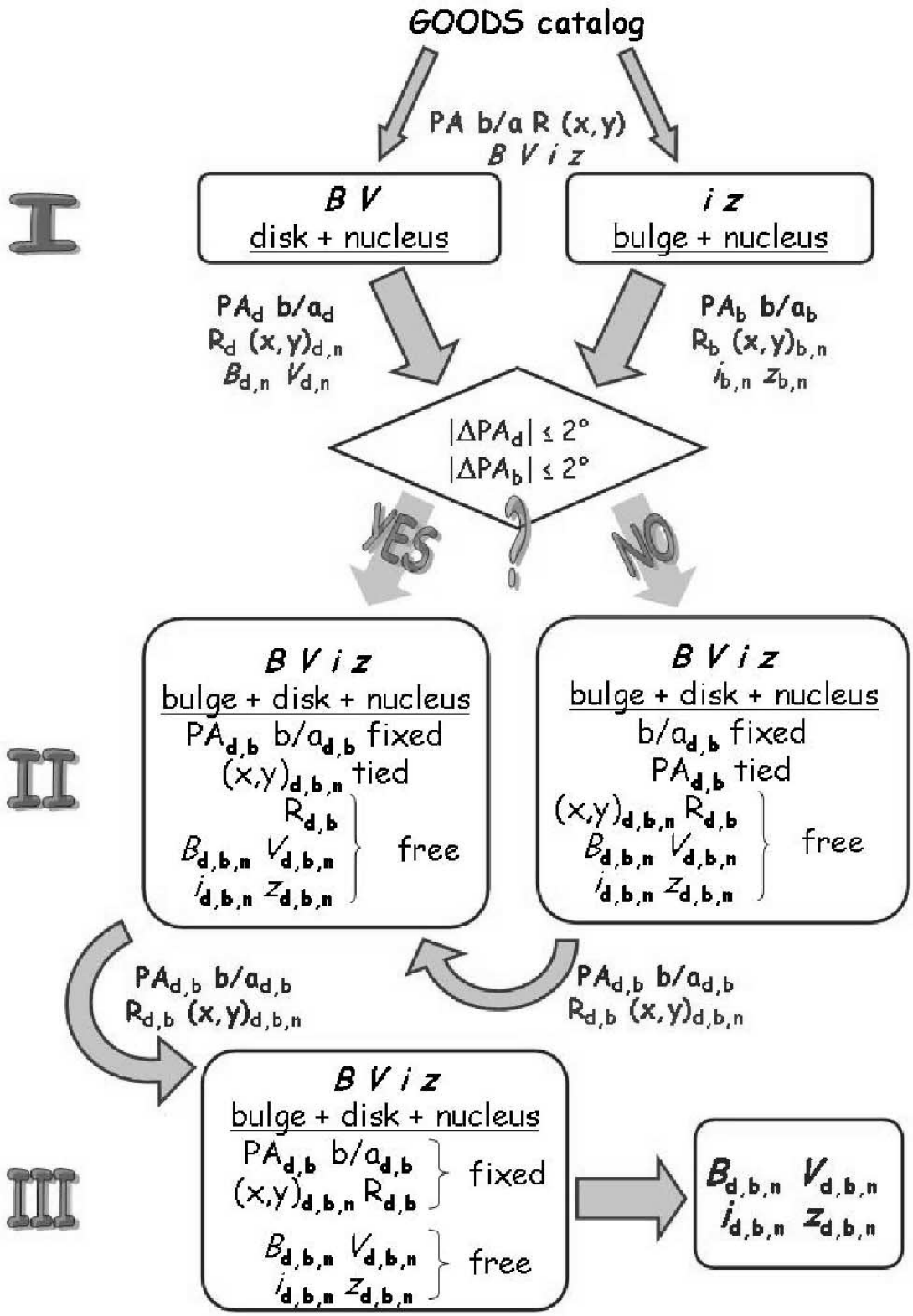

FIG. 11.—Flux diagram showing the various steps of the performed decomposition. Square boxes indicate a single run of GALFIT; parameters subject to a check are implemented in the rhomboidal boxes. Quantities near plump arrows connecting two boxes indicate the introduction from the starting box of new guesses (labeled as "free" or "tied" in the box of arrival) or fixed values for the corresponding parameter, respectively. Subscripts "*n*," "*b*," and "*d*" indicate parameters of the nucleus, bulge, and disk components. [*See the electronic edition of the Journal for a color version of this figure.*]

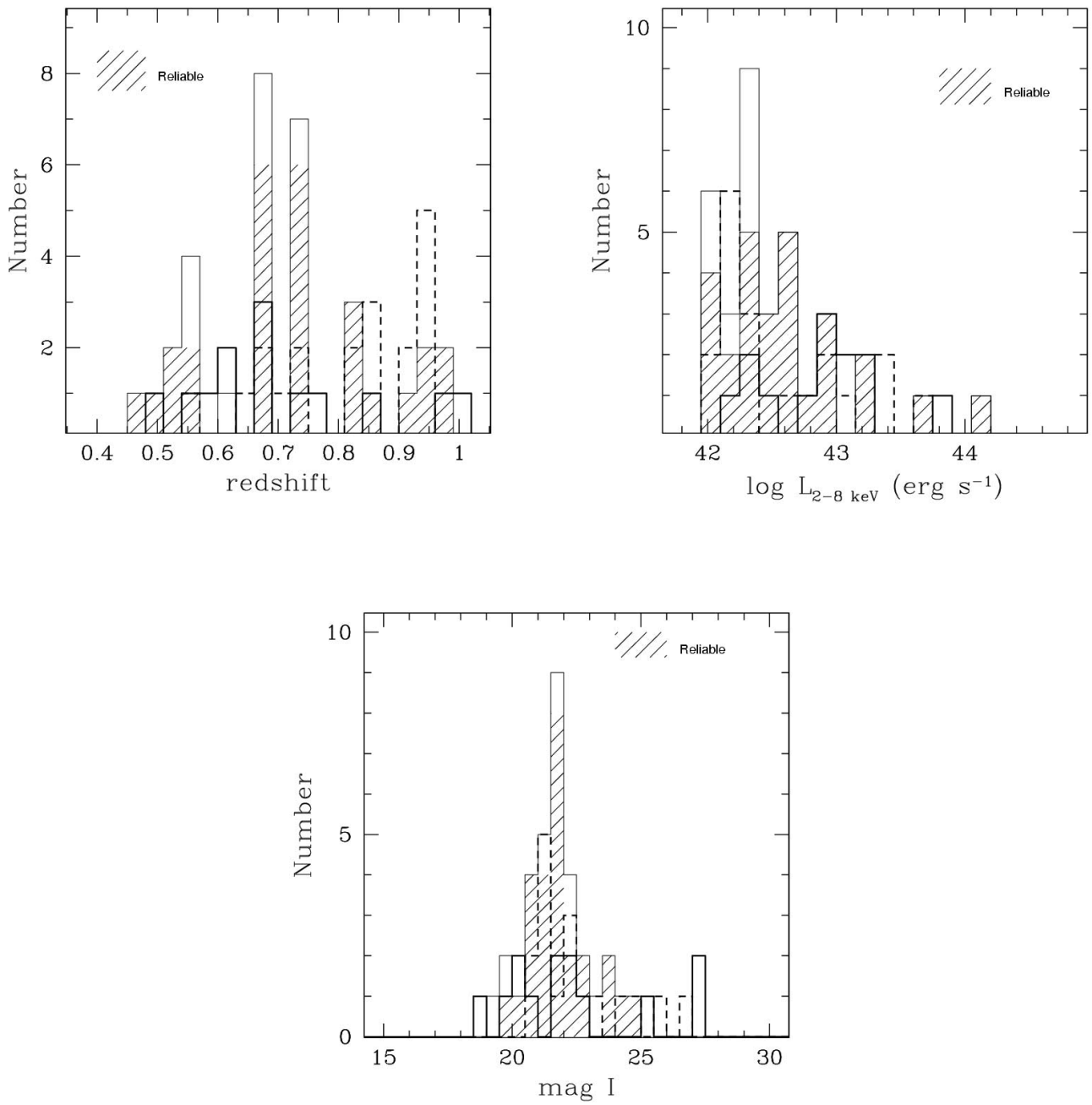

FIG. 12.—Distributions in redshift (*top left panel*), hard X-ray luminosity (*top right panel*), and *i*-band magnitude (*bottom panel*) for three subsamples of the GOODS X-ray sources with spectroscopic or photometric redshifts between 0.4 and 1 and observed hard X-ray luminosity $L_{2-8\,\mathrm{keV}} > 10^{42}$ ergs s^{-1}: sources with at least one bad cutout (*thick solid line*); sources not isolated, as defined in Appendix B (*dashed line*); analyzed sources (sample B, *thin solid line*); hatched areas show the same distributions for the sources for which we are confident that the results from the morphological decomposition are reliable. Redshifts are from Szokoly et al. (2004), Grazian et al. (2006), and Zheng et al. (2004) for the CDF-S, and from Barger et al. (2003) for the CDF-N; luminosities are from Alexander et al. (2003); and *i*-band magnitudes are from the GOODS ACS catalog (see footnote 12). [*See the electronic edition of the Journal for a color version of this figure*.]

REFERENCES

Alexander, D. M., et al. 2003, AJ, 126, 539
Arnouts, S., et al. 2001, A&A, 379, 740
Barger, A. J., et al. 2003, AJ, 126, 632
Bauer, F. E., Alexander, D. M., Brandt, W. N., Schneider, D. P., Treister, E., Hornschemeier, A. E., & Garmire, G. P. 2004, AJ, 128, 2048
Beckwith, S. V. W., et al. 2003, BAAS, 35, 723
Bender, R., Burstein, D., & Faber, S. M. 1992, ApJ, 399, 462
Bergvall, N., Laurikainen, E., & Aalto, S. 2003, A&A, 405, 31
Bernardi, M., Sheth, R. K., Tundo, E., & Hyde, J. B. 2007, ApJ, 660, 267
Bettoni, D., Falomo, R., Fasano, G., & Govoni, F. 2003, A&A, 399, 869
Brand, K., et al. 2005, ApJ, 626, 723
Brandt, W. N., et al. 2001, AJ, 122, 2810
Brusa, M., et al. 2003, A&A, 409, 65
———. 2005, A&A, 432, 69
Byun, Y. I., & Freeman, K. C. 1995, ApJ, 448, 563
Capak, P., et al. 2004, AJ, 127, 180
———. 2002, ApJ, 570, 114
Comastri, A., et al. 2002, ApJ, 571, 771
Cristiani, S., & Vio, R. 1990, A&A, 227, 385
Cristiani, S., et al. 2004, ApJ, 600, L119
De Luca, A., & Molendi, S. 2004, A&A, 419, 837
Della Ceca, R., Braito, V., Cagnoni, I., & Maccacaro, T. 2001, Mem. Soc. Astron. Italiana, 72, 841
Elvis, M., et al. 1994, ApJS, 95, 1
Fabian, A. C. 2004, in Coevolution of Black Holes and Galaxies, ed. L. C. Ho (Cambridge: Cambridge Univ. Press), 447
Fasano, G., Cristiani, S., Arnouts, S., & Filippi, M. 1998, AJ, 115, 1400
Ferrarese, L., & Ford, H. 2005, Space Sci. Rev., 116, 523
Ferrarese, L., & Merritt, D. 2000, ApJ, 539, L9
Ferrarese, L., et al. 2006, ApJ, 644, L21
Fontanot, F., Cristiani, S., Monaco, P., Nonino, M., Vanzella, E., Brandt, W. N., Grazian, A., & Mao, J. 2007, A&A, 461, 39
Gebhardt, K., et al. 2000, ApJ, 539, L13
Giacconi, R., et al. 2002, ApJS, 139, 369
Giavalisco, M., et al. 2004, ApJ, 600, L93
Gilli, R., et al. 2003, ApJ, 592, 721
———. 2005, A&A, 430, 811
Granato, G. L., & Danese, L. 1994, MNRAS, 268, 235
Granato, G. L., De Zotti, G., Silva, L., Bressan, A., & Danese, L. 2004, ApJ, 600, 580
Granato, G. L., Silva, L., Monaco, P., Panuzzo, P., Salucci, P., De Zotti, G., & Danese, L. 2001, MNRAS, 324, 757
Granato, G. L., Zitelli, V., Bonoli, F., Danese, L., Bonoli, C., & Delpino, F. 1993, ApJS, 89, 35
Grazian, A., et al. 2006, A&A, 449, 951
Grogin, N. A., et al. 2005, ApJ, 627, L97
Hasinger, G., et al. 2001, A&A, 365, L45
Hopkins, P. F., Hernquist, L., Cox, T. J., Di Matteo, T., Martini, P., Robertson, B., & Springel, V. 2005, ApJ, 630, 705
Ishisaki, Y., Ueda, Y., Yamashita, A., Ohashi, T., Lehmann, I., & Hasinger, G. 2001, PASJ, 53, 445
Kollmeier, J. A., et al. 2006, ApJ, 648, 128
Kormendy, J., & Gebhardt, K. 2001, in AIP Conf. Proc. 586, 20th Texas Symp. on Relativistic Astrophysics, ed. J. C. Wheeler & H. Martel (Melville: AIP), 363
Kormendy, J., & Richstone, D. 1995, ARA&A, 33, 581
Kuraszkiewicz, J. K., et al. 2003, ApJ, 590, 128
McLure, R. J., & Dunlop, J. S. 2002, MNRAS, 331, 795
———. 2004, MNRAS, 352, 1390
Magorrian, J., et al. 1998, AJ, 115, 2285
Mainieri, V., et al. 2005, A&A, 437, 805
Marconi, A., & Hunt, L. K. 2003, ApJ, 589, L21
Marconi, A., Risaliti, G., Gilli, R., Hunt, L. K., Maiolino, R., & Salvati, M. 2004, MNRAS, 351, 169
Marshall, F. E., Boldt, E. A., Holt, S. S., Miller, R. B., Mushotzky, R. F., Rose, L. A., Rothschild, R. E., & Serlemitsos, P. J. 1980, ApJ, 235, 4
Merritt, D., & Ferrarese, L. 2001, MNRAS, 320, L30
Mobasher, B., et al. 2004, ApJ, 600, L167
Monaco, P., & Fontanot, F. 2005, MNRAS, 359, 283
Moran, E. C., Lehnert, M. D., & Helfand, D. J. 1999, ApJ, 526, 649
Moy, E., Barmby, P., Rigopoulou, D., Huang, J.-S., Willner, S. P., & Fazio, G. G. 2003, A&A, 403, 493
Peng, C. Y., Ho, L. C., Impey, C. D., & Rix, H. 2002, AJ, 124, 266
Peng, C. Y., Impey, C. D., Ho, L. C., Barton, E. J., & Rix, H.-W. 2006, ApJ, 640, 114
Press, W. H., Teukolsky, S. A., Vetterling, W. T., & Flannery, B. P. 1997, Numerical Recipes in C (Cambridge: Cambridge Univ. Press)
Risaliti, G., & Elvis, M. 2004, in Supermassive Black Holes in the Distant Universe, ed. A. J. Barger (Dordrecht: Kluwer), 187
Rosati, P., et al. 2002, ApJ, 566, 667
Salucci, P., Szuszkiewicz, E., Monaco, P., & Danese, L. 1999, MNRAS, 307, 637
Severgnini, P., et al. 2003, A&A, 406, 483
Shankar, F., Salucci, P., Granato, G. L., De Zotti, G., & Danese, L. 2004, MNRAS, 354, 1020
Shankar, F., Salucci, P., Granato, G. L., de Zotti, G., & Danese, L. 2005, in Growing Black Holes: Accretion in a Cosmological Context, ed. A. Merloni, S. Nayakshin, & R. A. Sunyaev (Berlin: Springer), 470
Silk, J., & Rees, M. J. 1998, A&A, 331, L1
Silva, L., Granato, G. L., Bressan, A., & Danese, L. 1998, ApJ, 509, 103
Spergel, D. N., et al. 2003, ApJS, 148, 175
———. 2007, ApJS, 170, 377
Strateva, I. V., Brandt, W. N., Schneider, D. P., Vanden Berk, D. G., & Vignali, C. 2005, AJ, 130, 387
Szokoly, G. P., et al. 2004, ApJS, 155, 271
Tozzi, P., and the CDF-S Team. 2001, in Where's the Matter?, ed. L. Tresse & M. Treyer (Garching: ESO), http://www.eso.org/datagw/prosati/cdfspub
Tozzi, P., et al. 2006, A&A, 451, 457
Tremaine, S., et al. 2002, ApJ, 574, 740
Tundo, E., Bernardi, M., Hyde, J. B., Sheth, R. K., & Pizzella, A. 2006, preprint (astro-ph/0609297)
Ueda, Y., Akiyama, M., Ohta, K., & Miyaji, T. 2003, ApJ, 598, 886
Ueda, Y., et al. 1999, ApJ, 518, 656
Vandame, B., et al. 2001, preprint (astro-ph/0102300)
Vanzella, E., et al. 2005, A&A, 434, 53
Vecchi, A., Molendi, S., Guainazzi, M., Fiore, F., & Parmar, A. N. 1999, A&A, 349, L73
Vestergaard, M. 2004, ApJ, 601, 676
Vestergaard, M., & Peterson, B. M. 2006, ApJ, 641, 689
Vignali, C., Brandt, W. N., & Schneider, D. P. 2003, AJ, 125, 433
Virani, S. N., De Robertis, M. M., & VanDalfsen, M. L. 2000, AJ, 120, 1739
Volonteri, M., Salvaterra, R., & Haardt, F. 2006, MNRAS, 373, 121
Wadadekar, Y., Robbason, B., & Kembhavi, A. 1999, AJ, 117, 1219
Warner, C., Hamann, F., & Dietrich, M. 2004, ApJ, 608, 136
Waskett, T. J., Eales, S. A., Gear, W. K., McCracken, H. J., Lilly, S., & Brodwin, M. 2005, MNRAS, 363, 801
Woo, J.-H., Treu, T., Malkan, M. A., & Blandford, R. D. 2006, ApJ, 645, 900
Woo, J.-H., & Urry, C. M. 2002, ApJ, 579, 530
Yu, Q., & Tremaine, S. 2002, MNRAS, 335, 965
Zamorani, G., et al. 1981, ApJ, 245, 357
Zezas, A. L., Georgantopoulos, I., & Ward, M. J. 1998, MNRAS, 301, 915
Zheng, W., et al. 2004, ApJS, 155, 73